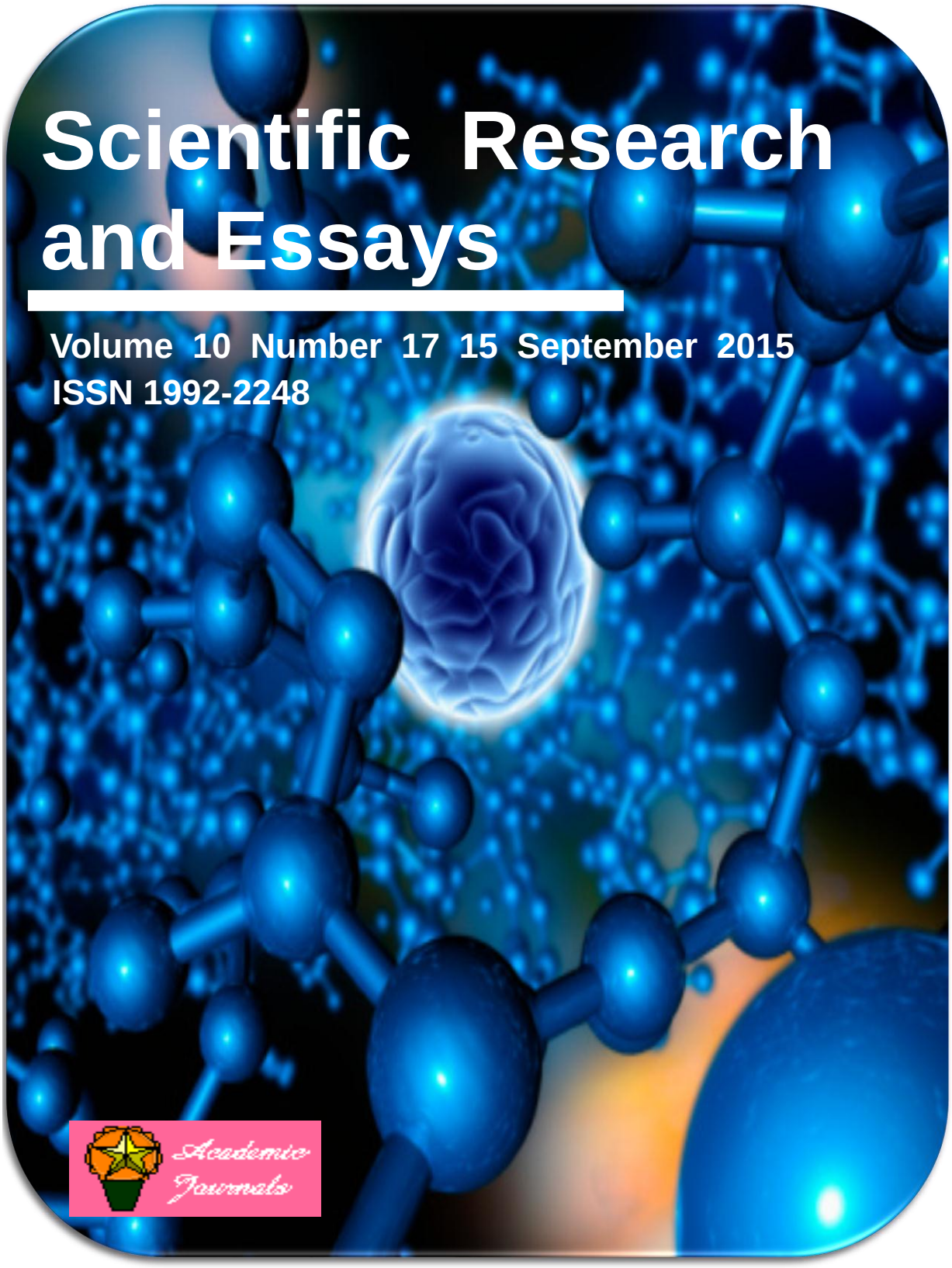

Scientific Research and Essays

Volume 10 Number 17 15 September 2015
ISSN 1992-2248

Academic Journals

ABOUT SRE

The **Scientific Research and Essays (SRE)** is published twice monthly (one volume per year) by Academic Journals.

Scientific Research and Essays (SRE) is an open access journal with the objective of publishing quality research articles in science, medicine, agriculture and engineering such as Nanotechnology, Climate Change and Global Warming, Air Pollution Management and Electronics etc. All papers published by SRE are blind peer reviewed.

Submission of Manuscript

Submit manuscripts as email attachment to the Editorial Office at sre@academicjournals.org. A manuscript number will be mailed to the corresponding author shortly after submission.

The Scientific Research and Essays will only accept manuscripts submitted as e-mail attachments.

Please read the **Instructions for Authors** before submitting your manuscript. The manuscript files should be given the last name of the first author.

Editors

Editorial Board

Fees and Charges: Authors are required to pay a $550 handling fee. Publication of an article in the Scientific Research and Essays is not contingent upon the author's ability to pay the charges. Neither is acceptance to pay the handling fee a guarantee that the paper will be accepted for publication. Authors may still request (in advance) that the editorial office waive some of the handling fee under special circumstances.

Submission of a Manuscript Implies: that the work described has not been published before (except in the form of an abstract or as part of a published lecture, or thesis) that it is not under consideration for publication elsewhere; that if and when the manuscript is accepted for publication, the authors agree to automatic transfer of the copyright to the publisher.

Scientific Research and Essays

Table of Contents: Volume 10 Number 17 15 September, 2015

ARTICLES

Research Articles

academicJournals

Vol. 10(17), pp. 531-543, 15 September, 2015
DOI: 10.5897/SRE2015.6248
Article Number: CD9CA3846875
ISSN 1992-2248

http://www.academicjournals.org/SRE

Scientific Research and Essays

Full Length Research Paper

Adaptive Pixel-Selection Fractional Chaotic Map Lattices for image cryptography

Jirasak Sittigorn* and Kitti Paithoonwattanakij

Faculty of Engineering, King Mongkut's Institute of Technology Ladkrabang, Chalongkrung Rd., Ladkrabang, Bangkok, 10520, Thailand.

Received 6 May, 2015; Accepted 20 July, 2015

Chaotic theory has been employed in cryptography application for establishing a sequence of data closest to pseudorandom number. Image cryptography with Chaotic Map Lattices (CML) uses the chaos parameters, the number of iterations and the number of cycles for encryption as secret keys. Amount of secret keys has a great impact on security in cryptography. Adaptive Pixel-Selection Fractional Chaotic Map Lattices (APFCML) enhances the encryption security by introducing a novel non-integer fractional order concept as secret keys. Fractional chaos is modified chaos with a fractional differential equation containing derivatives of non-integer order. A non-integer order has an effect on the range of chaos's parameter. Moreover, the encryption sequence has been adaptively selected based on another chaos generator. In the experiments, the measurement indices of originality preservation, visual inspection, and statistical analysis are used to evaluate the performance of the proposed APFCML compared to that of the original CML.

Key words: Chaotic, fractional logistic, image cryptography, Lyapunov exponent, bifurcation diagram.

INTRODUCTION

In the current trends, the communication is through the public network such as the Internet. The secure communication is crucial for business communication (Pecora and Carroll, 1990; Van Wiggeren and Roy, 1998). Electronic banking and military communication are two sample applications that clearly require a secure communication. The cryptographic algorithm is a method to protect plain text by changing it to data confidentiality. The cryptographic algorithm encrypts the plain text to a ciphered text using a key or keys, and it decrypts the ciphered text back to the plain text (Pareek et al., 2003).

Symmetric-key cryptography is algorithms for cryptography used the same keys for both encryption and decryption while asymmetric cryptography uses different keys for encryption and decryption. Since the symmetric-key cryptography shared keys when transforming a message back and forth, it becomes a target of attacking from an intruder. An attack can simply try different keys until the plain text is found.

The chaotic theory has been applied to the symmetric-key cryptography. It is a field of science that studies behavior of nonlinear dynamic systems that are highly

**Corresponding author. E-mail: jirasak@live.kmitl.ac.th.

sensitive to small variation of an initial condition. The output of a dynamic system is greatly deviated when initial conditions or parameters are changed. Therefore, initial conditions and system parameters are used as keys for the chaotic cryptography. The nature of a chaotic system makes a dictionary attack impractical. Chaotic Map Lattices (CML) (Pisarchik et al., 2006) is a cryptographic algorithm using the chaotic theory. Without knowledge of keys used in an encryption process, the decryption is practically difficult. The keys for the CML are chaotic parameters, number of iterations, and number of cycles. The parameters are variables in a logistic map that is well known chaotic systems. The limitation of a logistic map is the value of the parameter between 3.57 and 4. Therefore, a logistic map was chaos. When CML is applied to image cryptography, it encrypts and decrypts every pixel of an image. The CML algorithm uses an initial condition from the previous pixel in sequence for the current encrypting pixel. As a result, it is possible to decrypt all the sequence of the encrypted pixels if the intruder can guess secret keys and the initial condition of the first pixel. In order to enhance the encryption security, an Adaptive Pixel-Selection Fractional Chaotic Map Lattices (APFCML) algorithm is proposed, where the encryption sequence has been adaptively selected. Even though the intruder can guess the secret keys and the initial condition of the first pixel, it is quite difficult to acquire the whole encryption sequence. Another limitation of the CML algorithm is the amount of secret keys. The presented APFCML algorithm is based on fractional order and a parameter of fractional chaos with fractional-order as a new secret key. The fractional-order system is a dynamical system that can be modeled by a fractional differential equation containing derivatives of non-integer order (Monje et al., 2010). Fractional chaos is the chaotic system when fractional-order and the selected parameters are appropriate. Each fractional-order offers difference boundary of parameter. The remainder of this paper is organized as follows. The methodology section describes the chaotic system, the fractional order logistic model, lyapunov exponent, bifurcation diagram, fractional chaotic system, and encryption and decryption algorithm using APFCML.

METHODOLOGY

Chaotic system

A logistic map is the well known chaotic systems, which is a polynomial mapping of degree two, and is given by:

$$x_{n+1} = r x_n \left(1 - x_n\right) \tag{1}$$

Where x_n is the system variable, r is the parameter, n is the number of iterations and x_0 is an initial condition. The system variable and parameter lead to chaotic system when $x_{\min} < x_n < x_{\max}$, $3.57 < r < 4$, $x_{\max} = \frac{r}{4}$ and $x_{\min} = \frac{r^2}{4}\left(1 - \frac{r}{4}\right)$.

Fractional order logistic model

The fractional order logistic model was the mathematical form accomplished by integral and derivative of fractional order (Podlubny, 1999). This mathematical field may be considered as old topic since it is been developed for more than a century (Podlubny, 1999). Recently, this mathematical theory has applied to many modem applications in physics and engineer (Petras, 2006; Sabatier et al., 2007). The fractional order logistic equation is obtained by apply the fractional operator to the logistic equation as follow:

$$\frac{d^n x^\mu}{dx^n} = \frac{\Gamma\left(\mu + 1\right)}{\Gamma\left(\mu - n + 1\right)} x^{\mu - n} \tag{2}$$

Where $\Gamma(\ )$ is the Gamma function. The Gamma function is defined as $n! = \Gamma\left(n + 1\right)$.

The fractional order logistic model is operated by fractional derivative of logistic equation. The model is initially published by Pierre Verhulst (Pastijn, 2006). First order ordinary differential equation describes the continuous model. The discrete model discloses the chaotic property in certain regions (Alligood et al., 1996). The logistic Equation (1) is written as the sigmoid function as $f\left(x\right) = rx\left(1 - x\right)$.

The fractional order logistic equation is obtained by applies the fractional operator to the logistic equation as follows:

$$D_x^\alpha f(x) = \frac{r x^{1+\alpha}}{\Gamma\left(\alpha + 2\right)}\left(1 - \frac{2x}{\alpha + 2}\right) \tag{3}$$

Where $D_x^\alpha f(x)$ is the α order derivative of a function $f(x)$, r is parameter, α is fractional order when $-\infty < \alpha < \infty$.

The result of the fractional logistic equation becomes chaotic system at some of parameter. Figures 1 and 2 illustrates the results with the number of iterations n=1-6. It can be seen that the chaotic behavior trends of fractional logistic equation arises at parameter $r = 6$ for order $\alpha = \frac{1}{2}$ and parameter $r = 5$ for order $\alpha = \frac{1}{4}$. The Lyapunov exponent and bifurcation diagram are tools for indicating chaos system.

Lyapunov exponent

In mathematics, the Lyapunov exponent is quantified the average stability for describing the discrete dynamical system which can compute from the result of numerical simulation or a physical experiment (Alligood et al., 1996; Moon, 2004). The characteristics of Lyapunov exponents are analyzed by the linear stability of non periodic system. An indicator is the typical rate of exponential divergence of nearby trajectories (Alligood et al., 1996; Suansook and Paithoonwattanakij, 2014). This quantity is characterizes the rate of separation of nearby close trajectories. The differences of initial condition and trajectories are provided the different in rate of separation. The dynamic system predictability is determined by the largest Lyapunov exponent. The positive value of Lyapunov

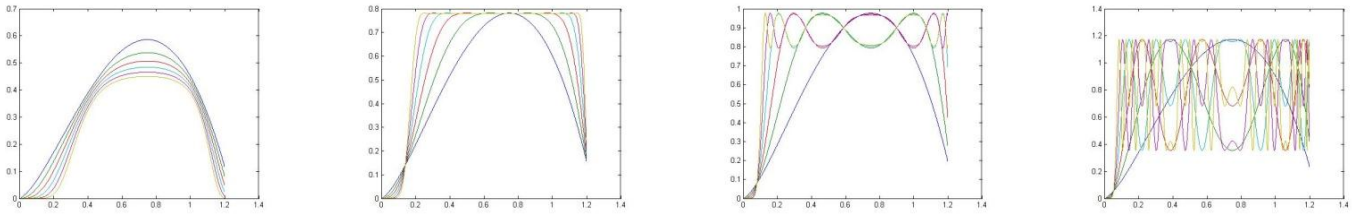

$r = 3$ $r = 4$ $r = 5$ $r = 6$

Figure 1. Result of fractional logistic equation for the number of iterations n=1-6 at order $\alpha = \frac{1}{2}$.

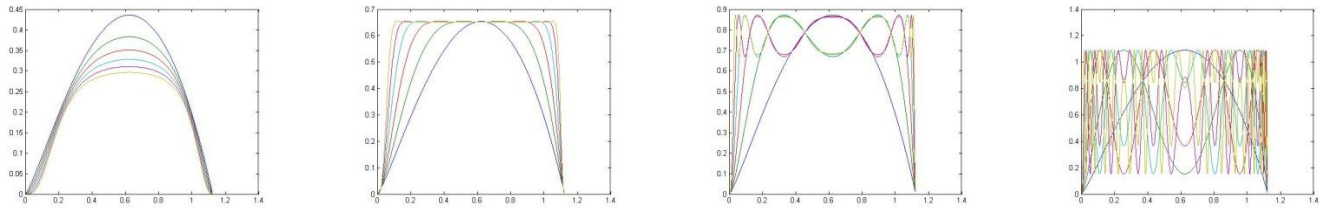

$r = 2$ $r = 3$ $r = 4$ $r = 5$

Figure 2. Result of fractional logistic equation for the number of iterations n=1-6 at order $\alpha = \frac{1}{4}$.

exponent is an indication that the system is chaotic (Alligood et al., 1996; Afraimovich and Hsu, 2002). The term Lyapunov exponent or exponential rate of divergence per iteration is defined as followed:

$$\lambda = \lim_{N\to\infty} \frac{1}{N} \sum_{n=1}^{N} \ln \left| \frac{df(x_i)}{dx} \right|_{x_i} \quad (4)$$

Where $\frac{df(x_i)}{dx}$ is the derivative of a function $f(x_i)$, λ is the Lyapunov exponent.

The Lyapunov exponent of fractional order logistic model can be calculated from the Equations (3) and (4). The numerical results of Lyapunov exponent of fractional logistic model for different order are shown in Figure 3.

Bifurcation diagram

Bifurcation theory was studies of changes in the qualitative of periodic point structure of dynamical systems, which is varying with time. The parameters are changed in a dynamical system, the stability of the balance points can change as well as the number of balance points. The values of parameters at which the qualitative or topological nature changes are known as critical or bifurcation values (Baker and Gollub, 1990). This occurs where a linear stability analysis yields an instability which characterized by a growth rate of a perturbation of the base solution. In dynamical system, a bifurcation diagram shows the possible long-term values either fixed points or periodic of a system as a function of a bifurcation parameter. In general, the bifurcation diagram represents stable solutions with solid line and unstable solutions with a dotted line. The theory of bifurcation is to study how the equilibrium points changes with the parameters (Suansook and Paithoonwattanakij, 2006). The bifurcation diagrams of the fractional order logistic equation for different order are illustrated in Figure 4.

Results of Lyapunov exponent and bifurcation diagram for each fractional order are used to describe the chaotic of fractional order logistic equation. The equation become chaotic when Lyapunov exponent value is greater than zero or Bifurcation Diagram are many values at the either fixed point (Table 1).

Image cryptography with regular CML considers the chaos parameters from a logistic map as one of secret keys. A logistic map becomes the chaotic system when the value of the parameter is between 3.57 and 4. However, in the proposed APFCML, the fractional logistic equation is chosen as additional secret keys. With dual sets of the secret keys, the encryption key length is extensive, thus the encryption security can be greatly intensifie.

The Lyapunov exponent and Bifurcation diagrams of fractional order logistic model are presented in Figures 3 and 4 respectively in order to illustrate the possibility of chaotic behavior in each fractional order. Even though the chaotic properties in fractional order logistic model depend on the same parameters as that of the logistic map, the order parameter is not restricted. Table 1 presents 10 samples of chaotic behavior cases with the order of fractional up to 9. With other fractional, the chaotic behavior can also be achieved. This leads to extensive selection of the fractional order parameters.

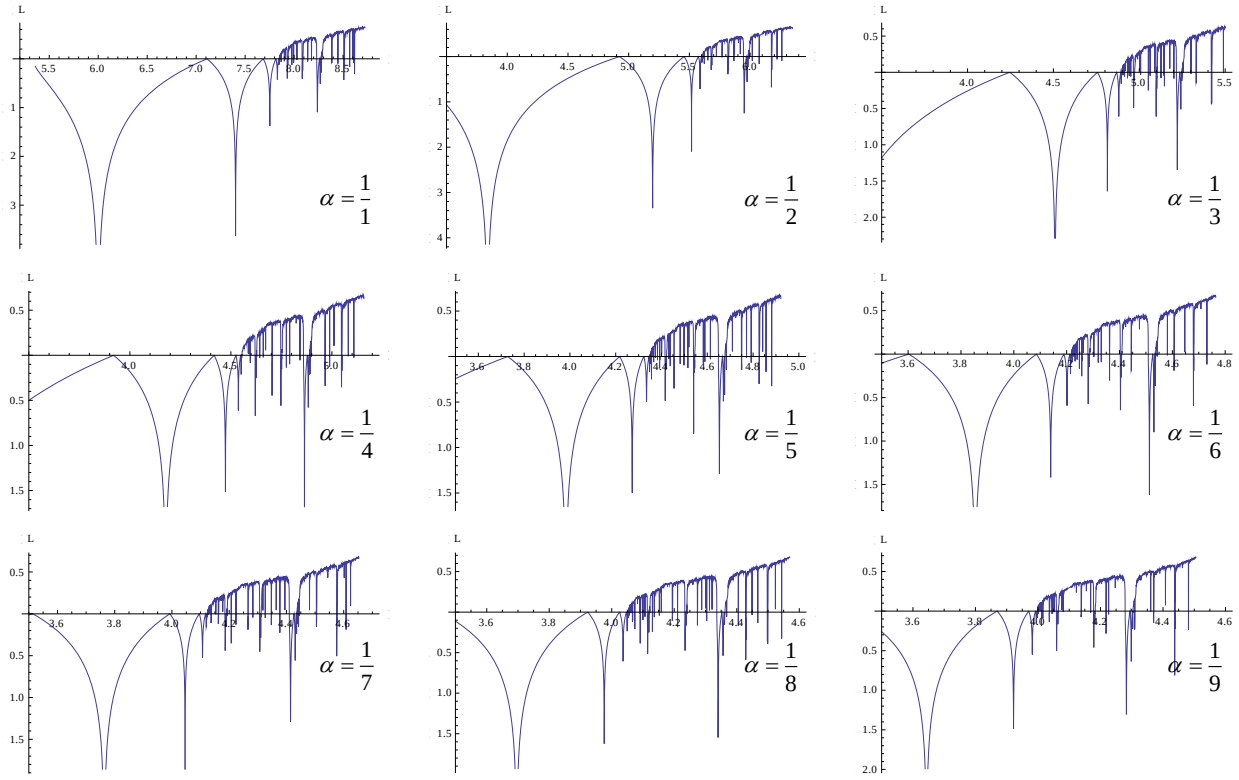

Figure 3. The Lyapunov exponent of fractional order logistic model at fractional order α .

Fractional chaotic system

The fractional logistic equation of order α in Equation (3) is rewritten in a logistic map as followed.

$$x_{n+1} = \frac{r x_n^{1+\alpha}}{\Gamma(\alpha+2)}\left(1-\frac{2x_n}{\alpha+2}\right) \tag{5}$$

Where x_n are the system variable, r is the parameter, n is the number of iterations x_0 is an initial condition and α is fractional order. For all $x \geq 0$ and $\alpha > 0$, $x_{\max}$ and $x_{\min}$ are as following.

$$x_{\max} = \frac{r(1+\alpha)^{1+\alpha}}{2^{1+\alpha}\Gamma(\alpha+2)}\left(1-\frac{\alpha+1}{\alpha+2}\right) \tag{6}$$

$$x_{\min} = \frac{r\left(\frac{r(1+\alpha)^{1+\alpha}}{2^{1+\alpha}\Gamma(\alpha+2)}\left(1-\frac{\alpha+1}{\alpha+2}\right)\right)^{1+\alpha}}{\Gamma(\alpha+2)}\left(1-\frac{2\left(\frac{r(1+\alpha)^{1+\alpha}}{2^{1+\alpha}\Gamma(\alpha+2)}\left(1-\frac{\alpha+1}{\alpha+2}\right)\right)}{\alpha+2}\right) \tag{7}$$

The image encryption, the image can be represented as a lattice of pixels. The color image is a combination of the three components: red, green, and blue shown as $C = (C_r, C_b, C_g)$. Encryption creates x_c by processing each of color component in parallel $x_c = (x_r, x_b, x_g)$. Normally, value of each component is an integer between 0 and 255. APFCML converts the integer value into the range of chaotic system variable by using the following transformation.

$$x_c = x_{min} + \delta x(C+1)/(257) \tag{8}$$

Where $\delta x = x_{\max} - x_{\min}$. To extract the value of color component, the inverse function is applied as followed:

$$C = \text{round}[(x_n - x_{min})(257)/\delta x - 1] \tag{9}$$

Where round is rounding function that replaces a numerical value to integer. With the modified normalization boundary, it results in complete recovery of the original pixel values.

Encryption and decryption algorithm

The revised encryption algorithm composes of the following steps.

Encryption algorithm

(1) Define secret keys as number of iteration (N), number of cycle (J). Define the new secret keys as fractional order α , parameter of fractional order r , chaotic parameters r_G and initial condition x_{G0} .

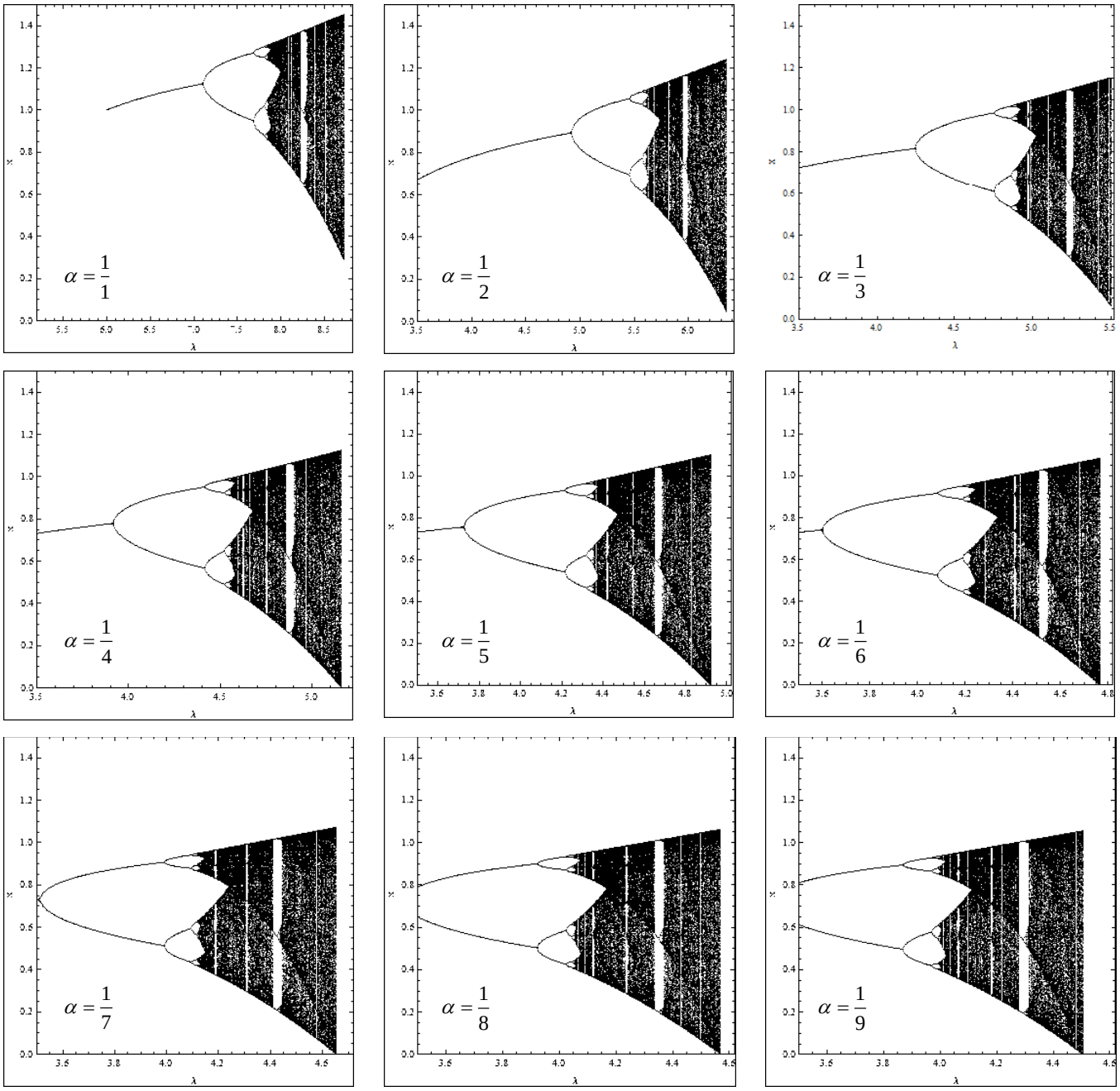

Figure 4. Bifurcation Diagram of fractional order logistic model at fractional order α .

(2) Convert two image containing two dimensional pixels (*Row*×*Column* = *m* pixels) into a sequential pixel of size m (i = 1, 2, 3, …, m), which its value is calculated in terms of variable C .

(3) Calculate sequential data m from the equation (1) with new secret keys (r_G and x_{G0}) in step 1). Sort sequential data as sequential pixels for encryption.

(4) Calculate x_C with Equation (8) of pixel *I* with new secret keys (α and r).

(5) Use the value of the last first element in sequential pixel in step 4) (x_c^{last}) as the initial condition for the first element in sequential pixel (x_0^{first}).

(6) Obtain the mapping variable x_n^{first} by iterating *N* times of the first element in sequential pixel from Equation (10). Add the mapping variable x_n^{first} and the value of pixel (x_c^{first}). The sum of value is applied as the initial condition for the subsequent order. Sometime, sum of value is over range of chaos system (x_{max}). We used the condition in Equation (12) to solve the problem. Iterate all maps subsequently starting from the first element in sequential pixel and going through encrypt image pixels, pixel by pixel, toward the last element in sequential pixel. The new x_c is the latest result of this cycle.

Table 1. The rank of parameter for chaos system.

Fractional order	Parameter
1/1	7.85-8.72
1/2	5.61-6.35
1/3	4.90-5.5
1/4	4.55-5.15
1/5	4.35-4.92
1/6	4.22-4.77
1/7	4.13-4.65
1/8	4.05-4.57
1/9	4.00-4.51

(7) Use the last element in sequential pixel (x_c^{last}) of previous cycle in step 7) as an initial condition for the first element in sequential pixel in the new cycle. Repeat step 6) overall the number of cycles (J).
(8) Convert the sequence of encrypted data x_C back to the image containing two dimensional.

The encryption algorithm can be summarized as following Equations (10) to (12).

$$x_0^i(j) = x_c^{last}(j-1) \quad ;if \quad i = 1^{st} \tag{10}$$

$$x_0^i(j) = x_c^{i-1}(j) \quad ;if \quad i \neq 1^{st} \tag{11}$$

$$x_c^i(j) = \begin{cases} x_n^i(j-1) + x_c^i(j-1) & if \quad x_n^i(j-1) + x_c^i(j-1) \le x_{\max} \\ x_n^i(j-1) + x_c^i(j-1) - \delta x & if \quad x_{\max} < x_n^i(j-1) + x_c^i(j-1) \le 2x_{\max} - 2x_{\min} \\ x_n^i(j-1) + x_c^i(j-1) - 2\delta x & if \quad 2x_{\max} - 2x_{\min} < x_n^i(j-1) + x_c^i(j-1) \end{cases} \tag{12}$$

Decryption algorithm

The revised decryption algorithm is as followed.

(1) Use secret keys from Encryption Algorithm as parameter, number of iteration, number of cycle and the new secret keys in step 1).
(2) Convert the encrypted image containing two dimensional in terms of sequence encrypted data x_c.
(3) Calculate sequential data *m* from the Equation (1) with new secret keys in step 1). Sort sequential data as sequential pixel for decryption.
(4) Recover the image of the *j*-1 cycle. Start decryption at the last element in sequential pixel by using previous order pixels ($x_c^{i-1}(j)$) as initial condition $x_0^i(j-1)$. Calculate $x_n^i(j-1)$ at N iterations from the Equation (5). Subtract the last element in sequential pixel $x_c^i(j)$ by $x_n^i(j-1)$. Continue decryption process to the first element in sequential pixel.
(5) Apply the last element in sequential pixel of j-1 cycle as the initial condition at the first element in sequential pixel ($x_0^{first}(j-1)$). After N iterations from (1) $x_n^{first}(j-1)$. Subtract the first order $x_c^{first}(j)$ by $x_n^{first}(j-1)$. The subtraction value is used as the initial condition for the next element in sequential pixel. Sometime, the subtraction of value is under range of chaos system (x_{min}). We propose the new condition in Equation (14).
(6) Repeat steps (4) to (5) for the next cycles until cycle *j*=0.
(7) Convert the decrypted data x_C back to the image containing two dimensional and then convert to the original image with formula (8) (Figure 5).

The decryption algorithm can be summarized as follows in Equation (13) to (15)

$$x_0^i(j-1) = x_c^{i-1}(j) \quad ;if \quad i \neq 1^{st} \tag{13}$$

$$x_0^i(j-1) = x_c^{last}(j-1) \quad ;if \quad i = 1^{st} \tag{14}$$

$$x_c^i(j-1) = \begin{cases} x_c^i(j) - x_n^i(j-1) & if \quad x_c^i(j) - x_n^i(j-1) \ge x_{\min} \\ x_c^i(j) - x_n^i(j-1) + \delta x & if \quad -x_{\max} + 2x_{\min} \le x_c^i(j) - x_n^i(j-1) < x_{\min} \\ x_c^i(j) - x_n^i(j-1) + 2\delta x & if \quad 2x_c^i(j) - x_n^i(j-1) < -x_{\max} + 2x_{\min} \end{cases} \tag{15}$$

ANALYSIS AND TEST RESULTS

Visual inspection

The encryption motivates the changes in pixel values without visual perception. Encryption quality is measured on how much changes can be introduced with minimum visual recognition. It can be measured as subjective test or objective tests in terms of statistical analysis such as histogram analysis, correlation analysis, cross-correlation analysis, and Gray Modification Average Value. The employed secret keys for the CML based encryption are the logistic map parameters, the number of iterations, and the number of cycles while fractional order parameters of the logistic model are additionally introduced in the proposed APFCML based encryption. In order to illustrate the comparative encryption quality of both encryption systems, the examples of experimental results obtained from the CML based encryption with $r = 3.90$ and those obtained from the proposed APFCML based encryption with $\alpha = \frac{1}{2}, r = 5.90$ are presented in Figure 6. Both encryption systems are compared with the same number of iterations and the number of cycles. Figure 6 shows the encrypted Lena images with ten combination of the number of iterations and the number of cycles of J = 1, N = 1-5 and J = 2, N = 1-5.
From the results, it can be seen that the CML and the APFCML deliver high encryption quality when the number of cycles is greater than 1. Observing the encrypted images with number of cycles is 2 and the number of iterations is 1 that the CML have Lena image information more than the APFCML. The APFCML is more efficiency than the CML.

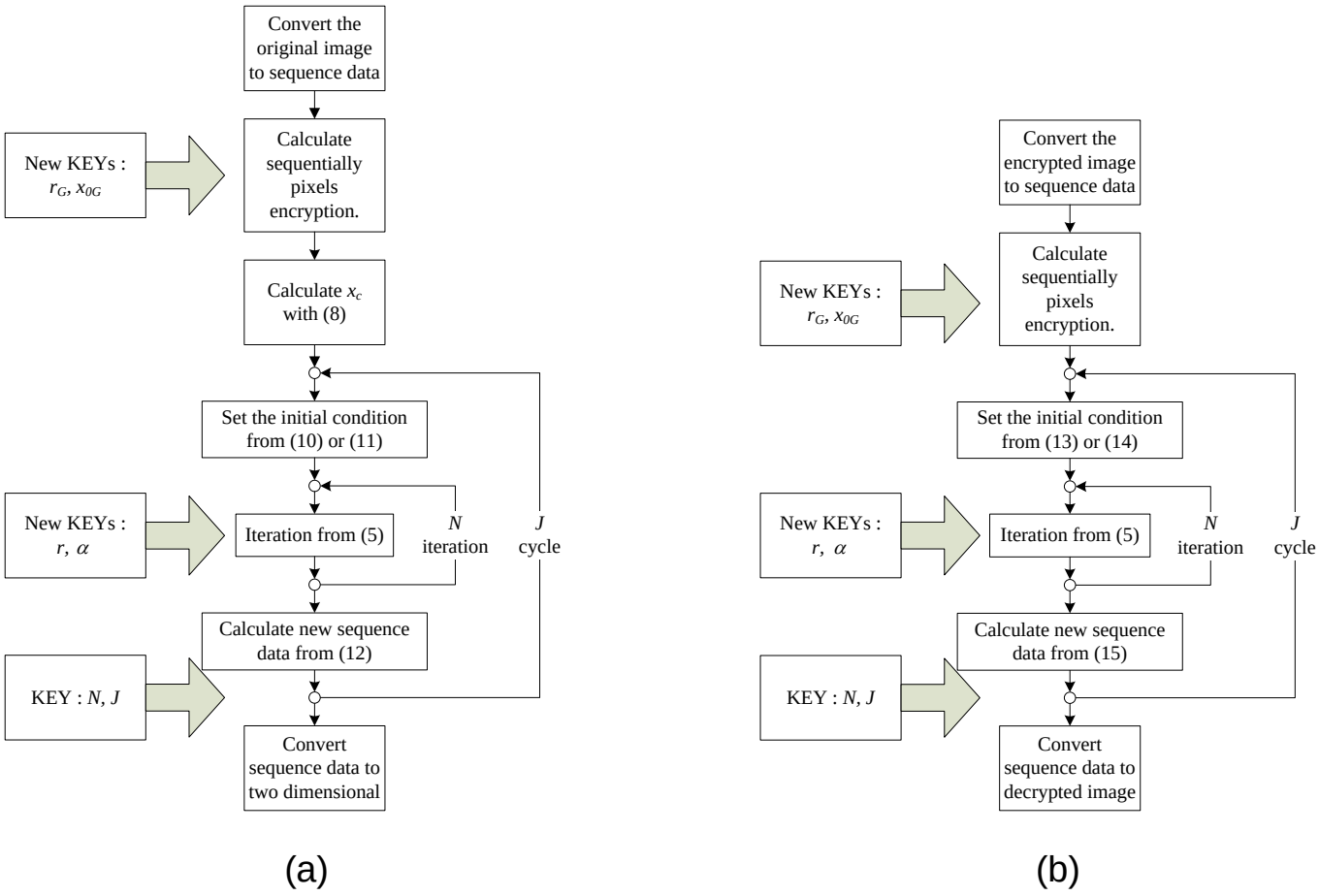

Figure 5. Block diagram for (a) encryption algorithm and (b) decryption algorithm.

Statistical analysis

The statistical analysis was analyzed in image encryption (Pareek et al., 2006; Liu et al., 2009). An encryption result should be robust against any statistical attack. The histograms of the test images and the correlations of two adjacent pixels in the encrypted images are simulated for statistical analysis.

Histogram analysis

It is important to verify that there is no statistical similarity between the encrypted and original images in order to prevent the leakage of information to the attackers. The statistical similarity can be illustrated in term of histograms, which present the distribution of the pixel intensity in images. Histogram of the Lena original image is shown in Figure 7a. Figure 7(b-f) shows histogram of the encrypted image using CML at $r = 3.90$. Figure 7(g- k) shows histogram of the encrypted image using APFCML when $\alpha = \frac{1}{2}, r = 5.90$. The histogram of original image contains large fluctuation while that of the encrypted image is close to the uniform distribution. It is significantly different from the original image. This shows that no statistical similarity appears between the encrypted and the original images.

From the results, the histogram distribution of the CML based encryption is close to the uniform distribution when J is greater than 1 and J is equal to N while that of the proposed APFCML based encryption can accomplish the goal with the J = 1 N =2. It can be seen that the proposed APFCML based encryption can converge to the desired distribution with lower order of the secret key parameters, thus it can allow extensive range of the encryption parameters. This can guarantee that the encryption with the proposed APFCML based system can achieve greater encryption security than that of the CML based system.

Correlation coefficient analysis

The correlation coefficient analysis is one of the important statistical analysis tools, which measures the statistical

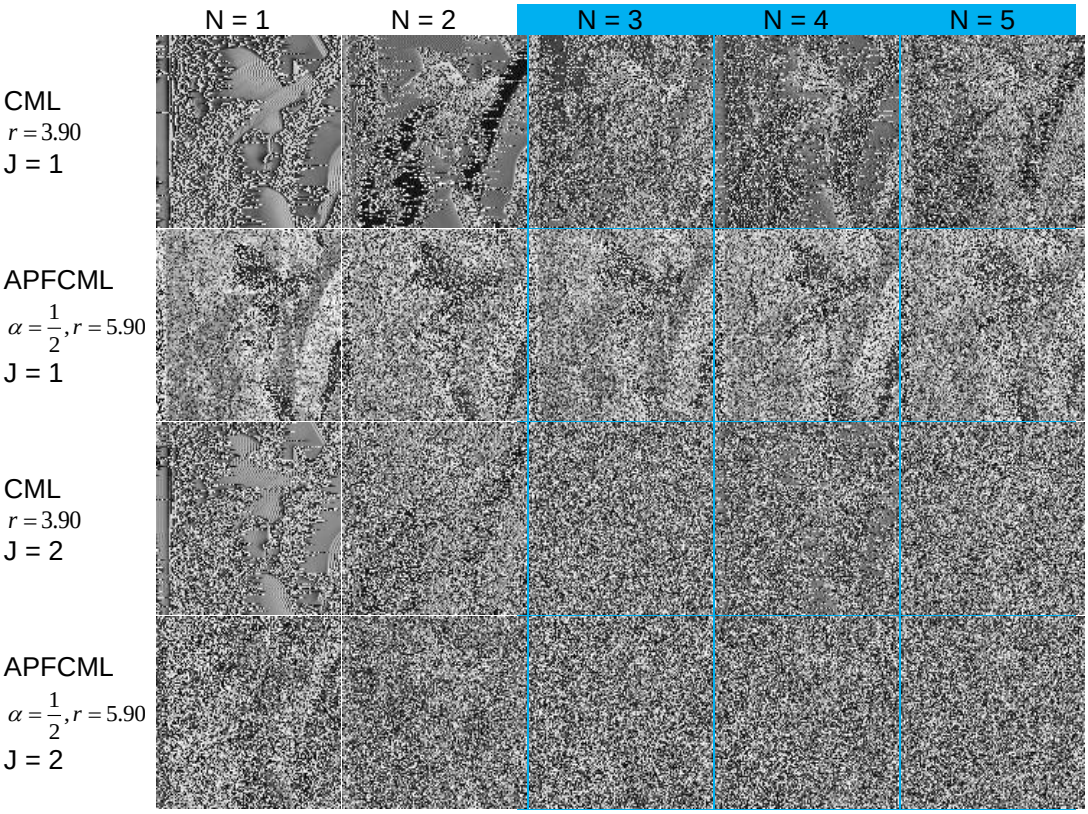

Figure 6. The encrypted Lena image with CML $r = 3.90$ and APFCML $\alpha = \frac{1}{2}, r = 5.90$.

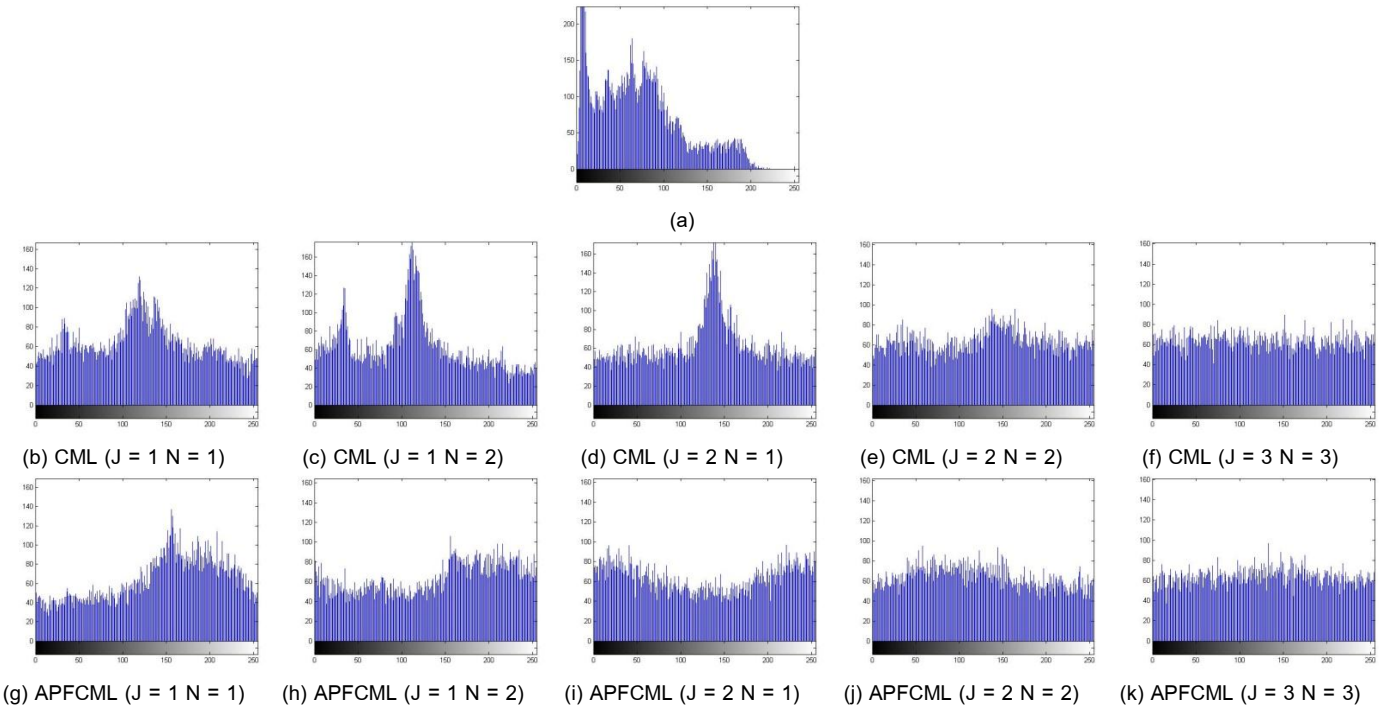

Figure 7. Histogram of (a) the original image and the encrypted image (b)-(f) CML $r = 3.90$ (g)-(k) APFCML $\alpha = \frac{1}{2}, r = 5.90$.

relationship between two horizontally adjacent pixels and two vertically adjacent pixels in encrypted image (Pareek et al., 2006; Liu et al., 2009). For effective image cryptography, all the attributes of the original images should be concealed, and the encrypted images should be highly uncorrelated. If the original and encrypted images are uncorrelated or totally different, their correlation will be very low or close to zero. If they are identical, their corresponding correlation will be equal to one. Figure 8 shows the distribution of two vertically adjacent pixels and two horizontally adjacent pixels. Figure 8(a) shows the distribution of the original Lena image. Figure 8 (b, d, f, h, j) show the distribution of the encrypted Lena image from CML ($r = 3.90$). The distributions of the encrypted Lena image from APFCML ($\alpha = \frac{1}{2}, r = 5.90$) are shown in Figure 8(c, e, g, I ,k).

The determination of how well adjacent pixels are correlated is to consider the regression line representing the data. The horizontally and vertically adjacent pixels are considered highly correlated if the regression line passes through points on the scatter plot. Otherwise, they are considered less correlated. The results show that the distributions obtained from the proposed APFCML based encryption are greatly dispersed from the scatter line for all Js and Ns while those of the CML based encryption are dispersed when J and N are greater than 2. This means that the APFCML encrypted pixels are greatly uncorrelated and it results in less visual perception and higher encryption quality.

Cross-correlation equation

The cross-correlation technique is a method to estimate the displacement information of two consecutive images by comparing the similarity of a pair of image signals (Kocarev et al., 2004; Solak and Çokal, 2008). The cross-correlation between two vertically and two horizontally adjacent pixels in the original and encrypted images are calculated using Equation (10) (Pareek et al., 2006; Liu et al., 2009).

$$C_r = \frac{N\sum_{j=1}^{N}\left(x_j \times y_j\right) - \sum_{j=1}^{N} x_j \sum_{j=1}^{N} y_j}{\sqrt{\left(N\sum_{j=1}^{N} x_j^2 - \left(\sum_{j=1}^{N} x_j\right)^2\right) \times \left(N\sum_{j=1}^{N} y_j^2 - \left(\sum_{j=1}^{N} y_j\right)^2\right)}} \quad (16)$$

Where x_j is intensity of pixel at location (x, y), y_j is intensity of pixel at location ($x+1$, y) for the cross-correlation of two vertically and y_j is intensity of pixel at location (x, $y+1$) for the cross-correlation of two horizontally.

Figure 9(a) demonstrates correlation coefficient analysis with CML based encryption for vertical and horizontal directions with various combinations of N and J parameters. The correlation coefficient analysis with APFCML based encryption is shown in Figure 9(b-d). It can be seen that, to achieve the correlation less than 0.05 for all variations of N, it limits the values of J greater than 5 for the CML thus greater than 3 for the APFCML. From the results, it demonstrates that the APFCML permits larger variation of secret keys with higher encryption quality for all parameters.

The results from Figure 9(a) and (b) show the correlation coefficient for the CML at J = 1 N = 1 more than the correlation coefficient for the APFCML that accords with the results of the visual inspection and the histogram analysis.

Gray modification average value

The values of pixels in the image encryption have been changed from the original image. Visual testing can show contrast between the original image and the image encryption. The percentage of unchanged point represents percentage of pixels difference. Gray modification average value, called GAVE, can measure the change in value of image encryption. The higher the GAVE value, the better the encrypted image. GAVE is defined in Equation (22), where $G = \left(g_{ij}\right)_{M\times N}$ is the original image and $C = \left(c_{ij}\right)_{M\times N}$ is the image encryption (Li and Wang, 2011).

$$GAVE(G,C) = \frac{\sum_{i=1}^{M}\sum_{j=1}^{N}\left|g_{ij} - c_{ij}\right|}{MN} \quad (17)$$

GAVE of all pixels in the image are shown in Figure 10. For the CML, GAVE will increase when number of cycle increases and number of iterations is greater than 7. At J=1, GAVE tends to converge slower. This is supported by the visual inspection results where the original information can still be perceived. For the APFCML, value of GAVE swing at number of cycleless than 3. Result shown GAVE value of APFCML more than CML.

Conclusion

This paper proposes an adaptive pixel-selection fractional chaotic map lattices for image cryptography to enhance the encryption security and overcome the limitation of the original CML. In the APFCML based encryption, the fractional logistic equation is applied in cryptography, which provides new secret keys as fractional order. In addition, the encryption sequence has been adaptively

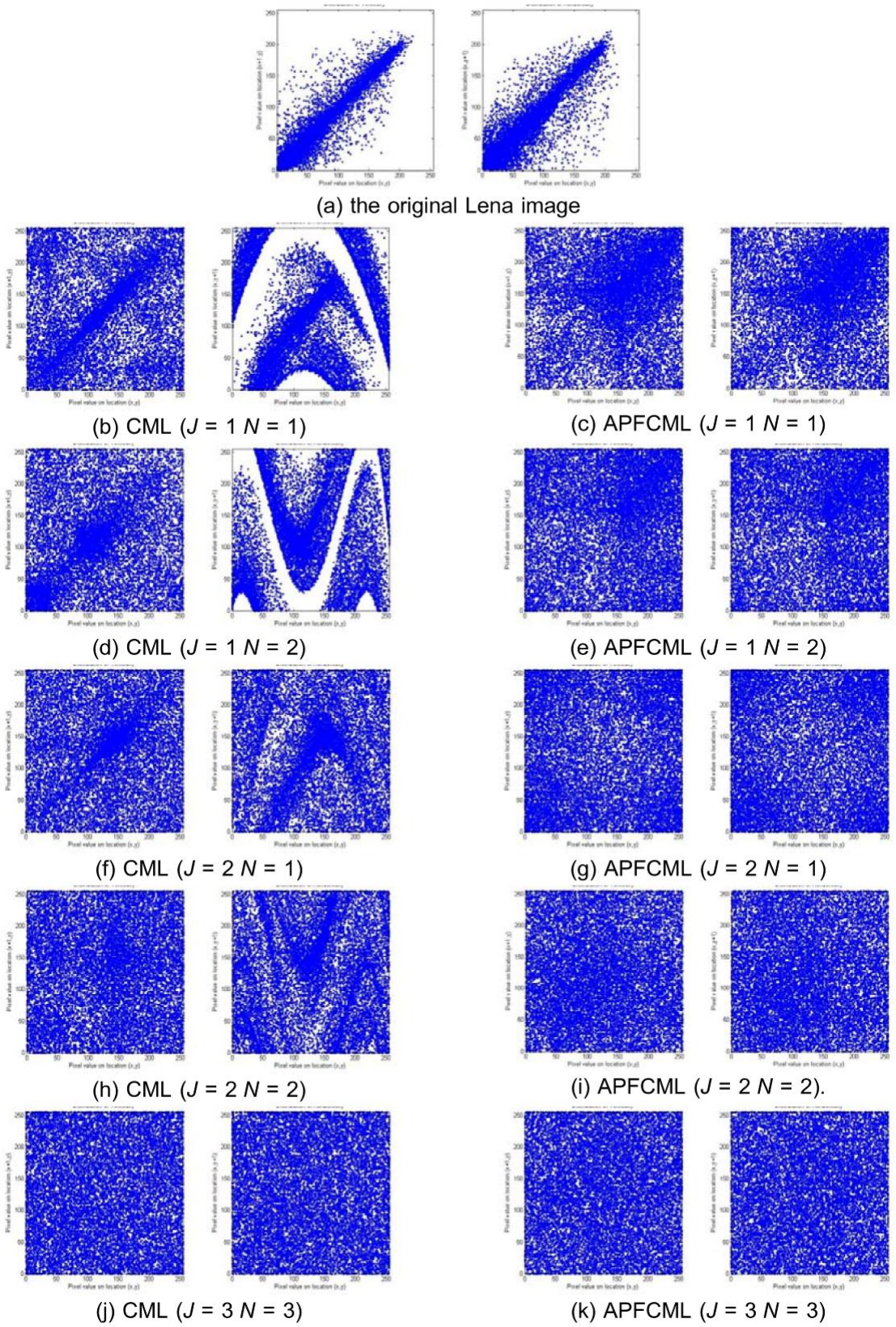

Figure 8. The distribution of two vertically adjacent pixels and two horizontally adjacent pixels of the original and encrypted Lena image with CML $r = 3.90$ and APFCML $\alpha = \frac{1}{2}, r = 5.90$.

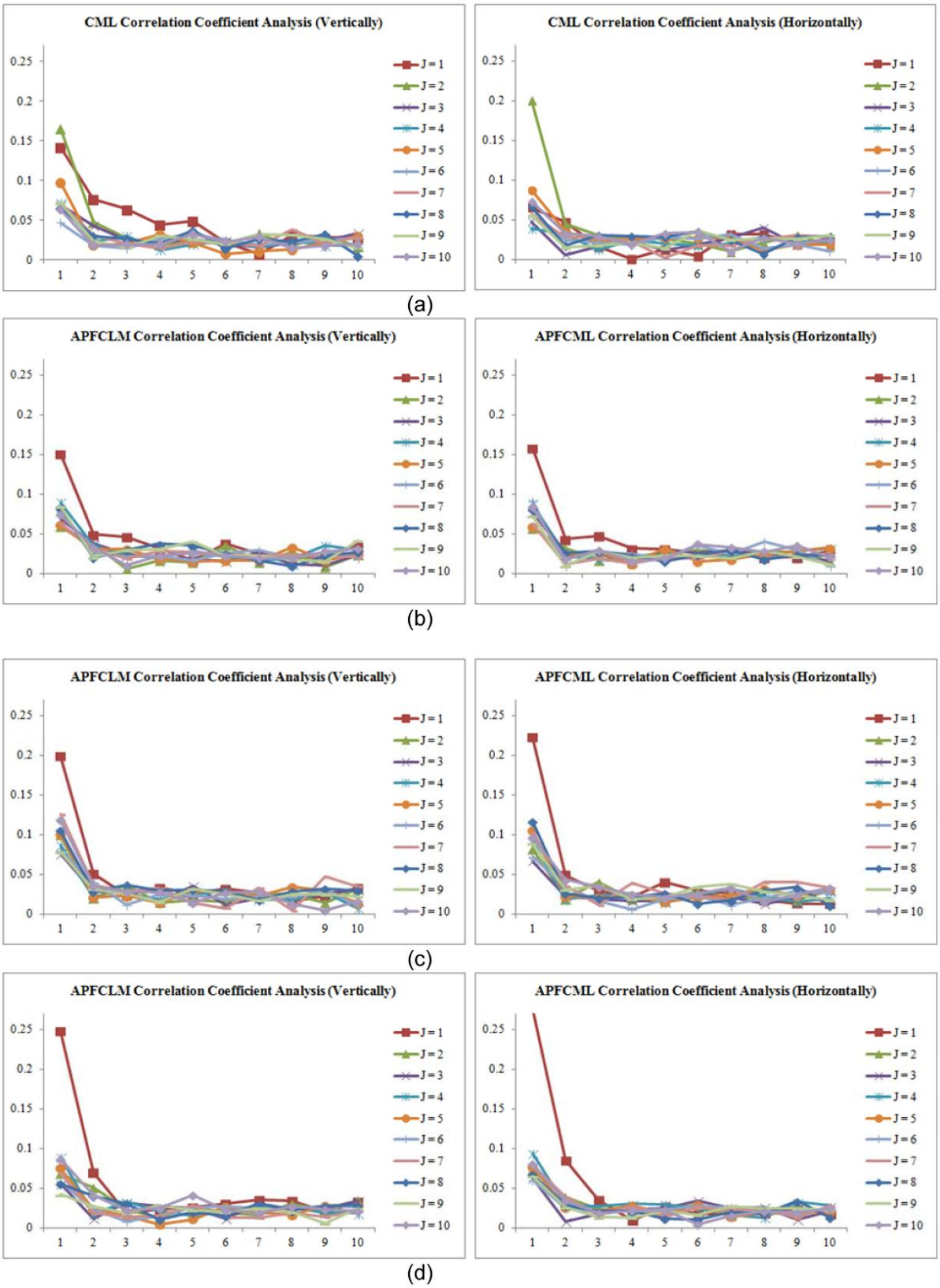

Figure 9. Correlation Coefficient Analysis for various combinations of *J* and *N* parameters of (a) CML $r = 3.90$ (b) APFCML $\alpha = \frac{1}{2}, r = 5.90$ (c) APFCML $\alpha = \frac{1}{2}, r = 5.97$ and (d) APFCML $\alpha = \frac{1}{4}, r = 4.85$.

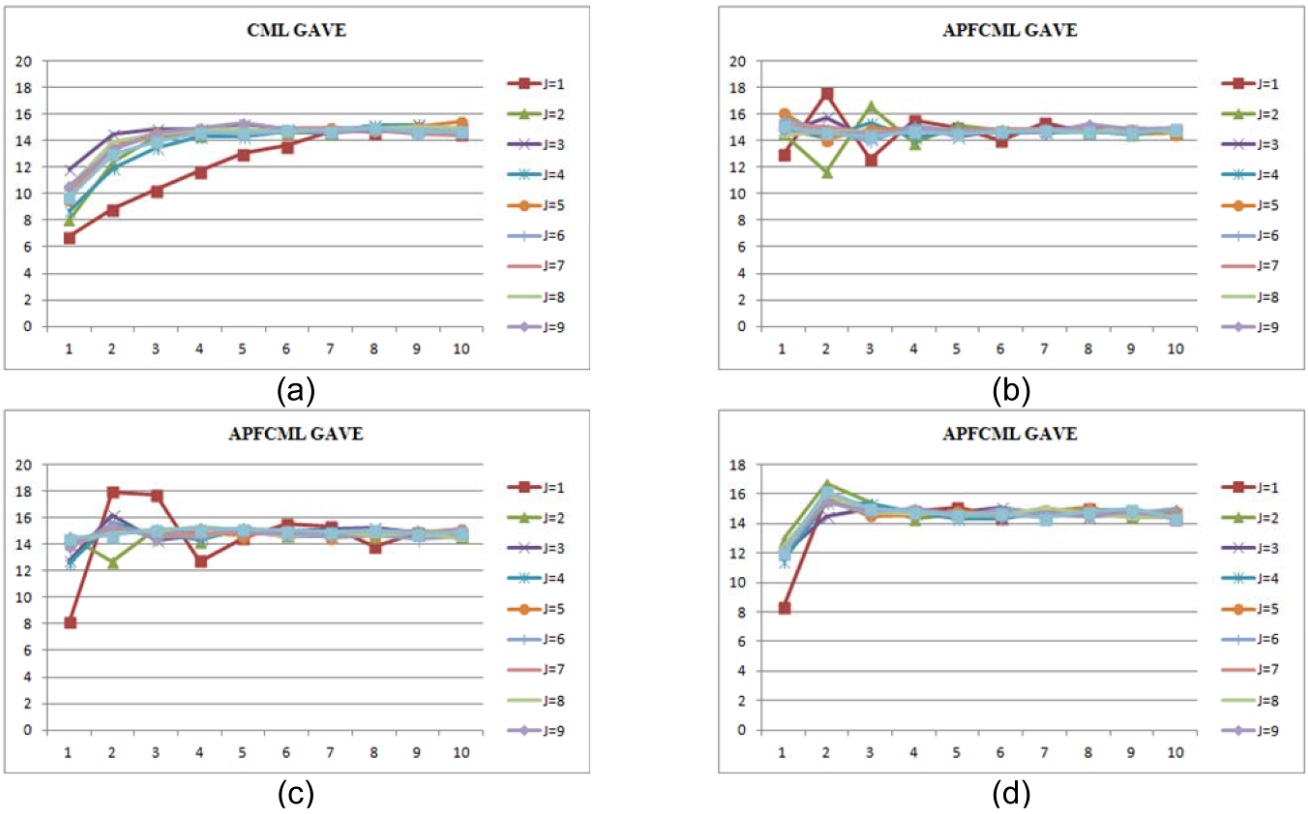

Figure 10. GAVE for various combinations of *J* and *N* parameters of (a) CML $r = 3.90$, (b) APFCML $\alpha = \frac{1}{2}, r = 5.90$, (c) APFCML $\alpha = \frac{1}{2}, r = 5.97$ and (d) APFCML $\alpha = \frac{1}{4}, r = 4.85$.

selected based on the chaos generator. Even though the intruder can guess the secret keys and the initial condition of the first pixel, it is quite difficult to acquire the whole encryption sequence. In the experiments, the measurement indices of originality preservation, visual inspection, and statistical analysis are used to evaluate the performance of the proposed APFCML compared to that of the original CML.

Conflict of Interest

The authors have not declared any conflict of interest.

REFERENCES

Afraimovich V, Hsu SB (2002). Lectures on Chaotic Dynamical Systems. American Mathematical Society. International Press.
Alligood KT, Sauer TD, Yorke JA (1996). An Introduction to Dynamical Systems. Springer.
Baker G L, Gollub J P (1990). Chaotic dynamics: an introduction. Cambridge University Press.
Kocarev L, Sterjev M, Fekete A, and Vattay G (2004). Public-key encryption with chaos. Chaos 14:1078-1082.
Li Q, Wang Y (2011). The Performance Analysis of Image Encryption Algorithm Based on Chaotic System. International Conference on Electronic & Mechanical Engineering and Information Technology. 978-I-61284-088-8/II/, pp. 3492-3494.
Liu S, Sun J, Xu Z (2009). An improved image encryption algorithm based on chaotic system. J. Comput. 4(11):1091-1100.
Monje CA, Chen Y, Vinagre BM, Xue D, Feliu-Batlle V (2010). Fractional-Order Systems and Controls: Fundamentals and Applications. Spinger. ISBN 9781849963350.
Moon FC (2004). Chaotic and Fractal Dynamics An Introduction for Applied Scientists and Engineers. Wiley-VCH Verlag GmbH and Co.
Pareek NK, Patidar V, Sud KK (2003). Discrete chaotic cryptography using external key. Phys. Lett. A. 309:75-82.
Pareek NK, Patidar V, Sud KK (2006). Image encryption using chaotic logistic map. Image Vision Comput. 24:926-934.
Pastijn H (2006). Chaotic Growth with the Logistic model of P.-F. Verhulst. Understanding Complex Systems, pp. 3-11.
Pecora LM, Carroll TL (1990). Synchronization in chaotic systems. Phys. Rev. Lett. 64:821-824.
Petras I (2006). Method for simulation of the fractional order chaotic systems. Acta Montanistica Slovaca. 11(4):273-277.
Pisarchik AN, Flores-Carmona NJ Carpio-Valadez M (2006). Encryption and decryption of images with chaotic map lattices. American Institute of Physics.
Podlubny I (1999). Fractional Differential Equations. New York: Academic Press.
Sabatier J, Agrawal OP, Tenreiro Machado JA (2007). Advances in Fractional Calculus Theoretical Developments and Applications in Physics and Engineering. Springer.

Solak E and Çokal C (2008). Comment on “Encryption and decryption of images with chaotic map lattices”. American Institute of Physics. DOI: 10.1063/1.2966114.

Suansook Y, Paithoonwattanakij K (2008). Bifurcation and Lyapunov Exponent in Orthogonal Frequency Division Multiplexing. IEEE 6th International Conference on Computational Cybernetics. Stara Lesná. Slovakia, pp. 107-112.

Suansook Y, Paithoonwattanakij K (2008). Chaos in Orthogonal Frequency Division Multiplexing Technique. International Conference on Advanced Computer Theory and Engineering, pp. 457-461.

Suansook Y, Paithoonwattanakij K (2014). Fractional order chaos in Josephson junction. Scientific Research and Essays. Vol.9(17):785-793.

Van Wiggeren DG, Roy R (1998). Communication with chaotic lasers. Science 279:1198-1200.

academicJournals

Vol. 10(17), pp. 544-548, 15 September, 2015
DOI: 10.5897/SRE2015.6260
Article Number: 8AF943D46886
ISSN 1992-2248

http://www.academicjournals.org/SRE

Scientific Research and Essays

Review

Evolutionary role of seed oils in plants: The case of *Jatropha curcas* L.

Isidro Ovando-Medina, Miguel Salvador-Figueroa and María de Lourdes Adriano-Anaya*

Instituto de Biociencias, Universidad Autónoma de Chiapas, Boulevard Príncipe Akishino s/n, Colonia Solidaridad 2000, Tapachula, 30798, Chiapas, Mexico.

Received 18 May, 2015; Accepted 21 August, 2015

Seed oils in higher plants function as an energy source for germination, emergence and establishing as a new plant. Then, the seed oil must be a trait subjected to natural selection. In this work we revise the evolutionary function of seed oils in angiosperms, analyzing the patterns of seed oil accumulation and their fatty acids composition among species differing in habit, habitat and relatedness. We review some relevant hypotheses about the evolutionary role of seed oils and their influence on plant fitness, using as case study the, apparently, inconsistent fatty acid profile of the tropical biofuel plant *Jatropha curcas* L. (Euphorbiaceae).

Key words: Fitness, tropical plants, selection factors, oleaginous plants, biofuels, Jatropha.

INTRODUCTION

The storage of oils in seeds is a generalized characteristic in higher plants, which has the main function of serve as an energy source to the embryo during the heterotrophic stage (Pujar et al., 2006), previous to the activation of the photosynthetic machinery. Such a stage is fundamental in the success or the failure of the embryo to germinate, emerge and establish as a new plant (Bewley and Black, 1994); therefore, seed traits like size, weight, thickness and hardiness of the coat, and the content of the endosperm determine, in part, the plant reproductive success. Then, the seed oil (considering the total content and the quality) must be a trait subjected to natural selection.

Probably not all the angiosperms accumulate large amounts of oil in their seeds, but this depends on the ecology and physiology of each species; however, even in the majority of the members of the most diverse family of plants, the Orchidaceae, which have tiny dust-like seeds lacking of endosperm (Vinogradova and Andronova, 2002) and, consequently, their seed reserves are scarce, the oil content can be as high as 32% of the seed weight (Arditti, 1967). Epiphytic orchids must produce too small seeds in order to colonize the canopy of forests (Prutsch et al., 2000), they need light during the germination, depend of mycorrhizal fungi for the initial growth and there is evidence of the inability of the embryo to use its oil reserves (oil droplets inside embryo cells) in absence of an external source of simple sugars (Manning and Staden, 1987). The cotyledons and endosperm disappearance seems to have led to the loss

*Corresponding author. E-mail: maria.adriano@unach.mx, Tel: +52-962-642-7972 (Ext. 100). Fax: +52-962-642-7972.

of several biochemical capabilities of orchid seeds (Arditti and Ernst, 1984), including the ability to catabolize oils. In cases like this probably the seed oil is not subjected to selection, but other seed characteristics, like the size and architecture.

To elucidate the evolutionary function of seed oils in plants two issues have been explored: the patterns in the total content and in the fatty acids composition of the oil among species differing in habit, habitat and relatedness. Thus, some hypotheses have been proposed to explain the patterns found.

There is a number of oleaginous plants accumulating seed oils; one of them is *Jatropha curcas*, a tropical plant native of the Mesoamerican region (Salvador-Figueroa et al., 2014). One interesting characteristic of this species is that their seed oil contains more than 70% of unsaturated fatty acids (Ovando-Medina et al., 2011), while most of tropical species have mainly saturated fatty acids, as the coconut oil (approximately 85% of saturated fats; Bezard et al., 1971) and the African oil palm (approximately 50% of saturation; Sambanthamurthi et al., 2000). Other species of *Jatropha*, such as *J. gossypifolia* have about 50% of unsaturated fatty acids (Hosamani and Katagi, 2008). Here, we review some relevant hypotheses centered in angiosperms and propose explanations for the apparently inconsistent fatty acid profile of the tropical biofuel plant *J. curcas* L. (Euphorbiaceae).

EXPLAINING THE PATTERNS IN THE TOTAL CONTENT OF OILS IN SEEDS

Seeds accumulate principally neutral oils (Lersten, 2006), that is, not volatiles, which are composed of triglycerides or three molecules of fatty acids attached to a molecule of glycerol through ester bonds (Coleman and Lee, 2004). Oil content can vary from around 1% in rice (*Oryza sativa* L.; Muzafarov and Mazhidov, 1997) to more than 55% in Myristaceae. Although determinations of oil contents have been realized since decades ago (Woodworth et al., 1952; Canvin, 1965), perhaps the first study searching for relations between ecological parameters and oil accumulation was that by Donald Levin in the seventies of the twentieth century. Implicitly, the bases of evolutionary function of seed oil were depicted.

Levin (1974) studied the relationships between seed oil content and plant habit and habitat (latitudinal origin and illumination of sites) of over one thousand species of angiosperms. He found that plants have increased their oil content concomitantly with the development of woodiness and shade tolerance, but there is no a pattern of variation in oil content as related to latitudinal origin (Figure 1).

Explanations to the patterns were related with the reproductive strategies (*r* or *K*) of the habit group. According to Levin, herbs, shrubs and trees accumulate progressively more seed oil, at the same time, they devote a gradually smaller proportion of their resources (counting, of course, reserves of oil) to reproduction, constituting gradually more *K*-selected forms. The author mentions that in tropics there is a prevalence of K-selected forms, leading to a selection of seeds rich in reserves. However, is its recognized that trees have characteristics of both *r* and *K*-selected organisms, because are perennials with high longevity at time produce large amounts of seeds.

Other simple explanation is that trees, living the first part of their life history in the understory, must accumulate more reserve lipids to have a strong initial growth; that's why the selection has acted on seeds with more oil content. To this respect, Ichie et al. (2001) demonstrated that germinating seeds of *Dryobalanops lanceolata* (Dipterocarpaceae), an enormous emergent tree of Borneo, use almost all their reserves to form a relatively big stem, which improve their establishing. The same is true for shade-tolerant species (Westoby et al., 1992). Studies analyzing the total content of seed oil of an arrangement of species, in a phylogenetic context, are needed in order to elucidate the evolutionary trends in this subject.

EXPLAINING THE PATTERNS IN THE FATTY ACID COMPOSITION

Seed oils are formed by an extension of the membrane-lipid biosynthetic pathway common to all plant tissues (Voelker and Kinney, 2001), but, in contrast to membrane lipids, there is great fatty acid diversity. The acyl chains of fatty acid range from 8 to 24 carbons, varying in degree of saturation (number of double bonds), spatial arrangement (*cis*, *trans*) and in functional groups. Many plant species accumulate seed oils with unusual fatty acids (Smith, 1970; Aitzetmüller et al., 1999; Dyer et al., 2002).

A huge amount of information is available on fatty acids diversity in plants, but the main interests are centered in the search for fingerprints useful in plant taxonomy (Sharma, 1993) and in the improvement for high accumulation of seed oils and for the production of novel (unusual) fatty acids or those industrially important (Hosamani and Katagi, 2008). Molecular biology tools are enabling to scientists to elucidate biochemical mechanisms implicated in the fatty acid diversity; for example, Dyer et al. (2002) demonstrated that a single divergent enzyme from *Aleurites fordii*, named FADX, can use the most common unsaturated fatty acids in plants (oleic, linoleic, and linolenic acids) to produce three different unusual fatty acids (as the 18:29*cis*, 12*trans*-eleostearic acid). This suggests a mechanism of accelerated evolution of plant fatty acids. Several other studies report the enzyme diversity involved in the fatty acid synthesis, using *Arabidopsis* and other plant models. Nowadays, we have a good level of knowledge of the biosynthetic pathways of

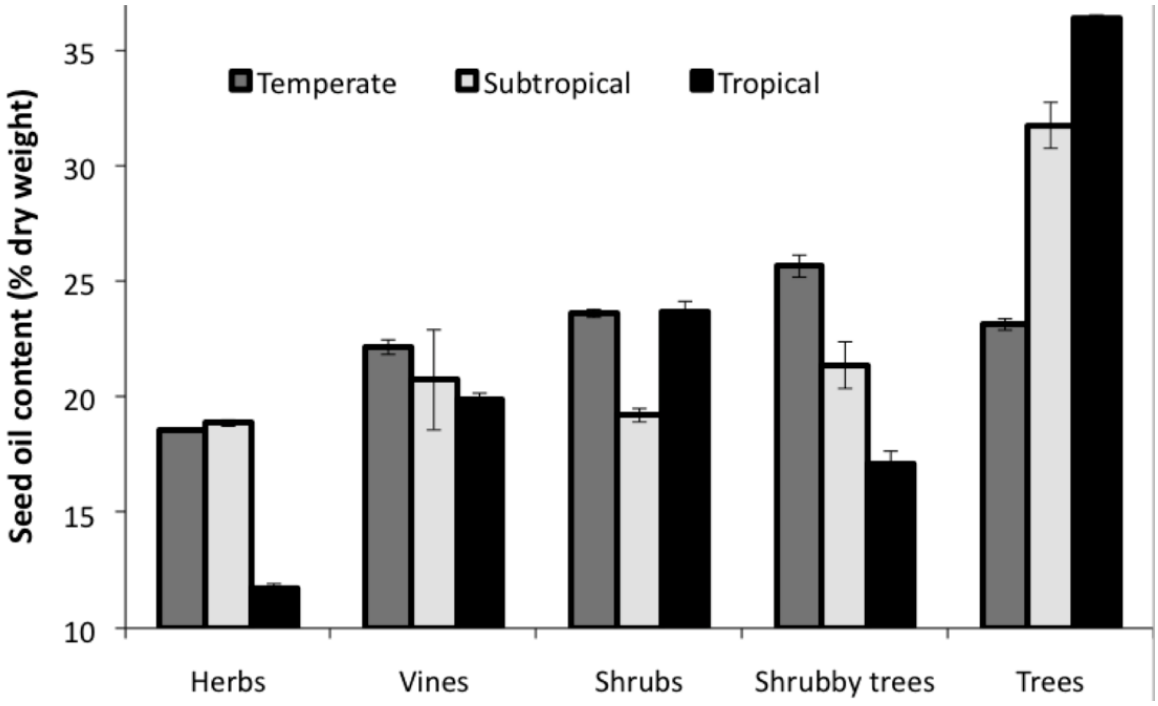

Figure 1. Non-phylogenetic comparison of seed oil contents of angiosperms of five habits and three ecological zones. Constructed with data from Levin (1984).

fatty acids in plants (White et al., 2000; Barker et al., 2007).

Surprisingly, little attention has been paid to the selection factors driving the evolution of the composition of fatty acids in seeds. To this respect, Linder (2000) proposed and tested a hypothesis to predict (and to explain) latitudinal and altitudinal variations in the ratio of saturated/unsaturated fatty acids in seed oils. Table 1 shows the premises and assumptions He used to construct his theory.

Linder (2000) suggested that germination temperature is an important selective agent causing seed oils of higher-latitude (or altitude) plants to have proportionately more unsaturated fatty acids than lower-latitude (or altitude) plants. This author designed elegant experiments to test the theory in both phylogenetic and non-phylogenetic contexts. Results showed the validity of the hypothesis at micro and macro-evolutionary scales.

Explanations to the above-mentioned patterns consist in that, in cooler environments (like those of higher latitude), the catabolism of unsaturated fatty acids is more feasible than that of saturated. As a consequence, seeds with more proportion of unsaturated fatty acids are able to germinate earlier and grow more rapidly at low temperatures (increasing their fitness) even though they store less total energy than seeds with more proportion of saturated fatty acids. It is important to take into account that in temperate zones optimal germination conditions are presented in well-defined periods of the year, then, seeds must germinate rapidly in such periods. On the other hand, in warm environments (like those of the tropics) seeds with higher proportions of saturated fatty acids are selectively favored because their oils will provide more energy, without a penalty in the rate of energy acquisition; germination conditions in tropics are more or less stable during the year.

THE CASE OF THE BIOFUEL PLANT *J. CURCAS* L.

J. curcas, also known in Southern Mexico and Guatemala as “Piñón”, is a euphorbiaceous plant with many uses across the world and a great potential in several fields. This plant probably is native to Mesoamerica; however, it currently exists as a crop in both the old and the new world, with excellent adaptation to tropical and subtropical regions. It is a multi-use species, but nowadays is being used to extract oil from its seeds to produce fatty acid methyl esters or biodiesel (Pramanik, 2003; Fairless, 2007).

Since the seed oil is the main product of that plant, many studies have explored the content and composition of the oil of seeds *J. curcas* from different parts of the tropics. Apparently, the total content (ranging between 20 and 50%; Heller, 1996) is in agreement with the Levin’s hypothesis because *J. curcas* can be considered a shrubby tree (the plant grows a maximum of 5 m). There are 175 species of *Jatropha* (Dehgan and Webster, 1979),

Table 1. Elements of the Linder's theory on the selection of saturated/unsaturated fatty acids of seed oils.

Premise	Consequences for the theory
Production and effects of triacylglycerols (TAGs) are exclusive of the seed stage	(i) TAGs are independent of the evolutionary forces acting in other plant's life history
Saturated fatty acids yields more energy than unsaturated	(ii) TAGs rich in saturated fatty acids should be selected
Some seed TAGs are low in saturated fatty acids	(iii) Something other than selection for maximum energy storage affect the rate saturated/unsaturated
Unsaturated fatty acids have low melting points	(iv) Under cooler temperature conditions unsaturated fatty acids are easily catabolized, then, seeds germinate rapidly
The germination temperature is the selective force influencing the rate saturated/unsaturated	(v) Unsaturated fatty acids should increase from low to high latitudes and altitudes
	(vi) Within a clade, species that germinate at cooler temperatures should have a low ratio saturated/unsaturated

Constructed with information from Linder (2000).

which vary in habit; it would be interesting to test the hypothesis of the correlation between the hardiness and the oil accumulation, but unfortunately information about oil determinations, if exists, is not available.

On the other hand, the composition of fatty acids of the seed oil of *J. curcas* appears to be in disagreement with the Linder's hypothesis because, being a tropical species, the selection has favored a major proportion of unsaturated fatty acids (Table 2).

Linder (2000) mentions alternative hypotheses to explain the latitudinal variation in accumulation of unsaturated fatty acids, but He discarded the herbivory and the photoperiod as the selection forces implicated. Probably, these factors do not explain the trend observed in *J. curcas*. He also mentions "*when the association between the proportion of saturated fatty acids and germination temperature does not hold, there should be either lack of genetic variation for oil composition within one or more species in the clade or other selection processes for alternate oil compositions*". We do not have enough data to analyze phylogenetically the saturated/unsaturated ratio in the genus *Jatropha* or even non-phylogenetically within *J. curcas* but, based in my chromatographic determinations of the fatty acids profiles of *J. curcas* from the Mesoamerican region (Ovando-Medina et al., 2011). We think there are other selection processes acting in this particular case.

We hypothesize that the soil humidity is pushing, al least in part, to select unsaturated fatty acids of the seed oil in *J. curcas*. It is well documented the tolerance of the species to drought; like other *Jatropha* species, the "piñón" has succulent stems and sheds its leaves during the dry season (Heller, 1996: Gubitz et al., 1999), although it grows well in a range of environments (from humid to semi-arid/arid tropical and subtropical) with optimal annual rainfalls between 300 and 1000 mm. However, it can grow and develop in areas with much more precipitations, if the soil drainage is good (Heller, 1996).

Nevertheless, the plant (and of course the seedling) is susceptible to the inundation; our personal observations of seedlings survival in the State of Chiapas (in the most Southern part of Mexico) showed that a few days of constant flood cause the death of seedlings and fifteen or more days could cause the death of an adult plant. In tropical zones, the flowering and fruiting of *J. curcas* is achieved during the non-rainy season and at the start of the rainy season; seeds do not present dormancy and germinate fast (typically in five days) and in high percentage. According to Dehgan and Schutzman (1994) *J. curcas* is present in South America in seasonally dry tropical areas, but are completely absent in the moist Amazon region.

If these observations are generalized facts, taking into account the energetic and catabolic properties of the fatty acids, a seed of drought tolerant plant with more unsaturated fatty acids can germinate and establish rapidly and with more probabilities to survive in a high precipitation zone than one with high proportion of saturated fatty acids. The excess of humidity could be other selection force in favor of a high proportion of unsaturated fatty acids.

CONCLUSION

In order to clarify the evolutionary function of seed oils in plants and to identify more assertively the selection factors driving the patterns in accumulation of oil and in the proportions of saturated/unsaturated fatty acids, it would be interesting to test the Linder's hypothesis in clades distributed along an altitudinal gradient. Besides, it is indispensable the analysis of total content of oils in a phylogenetic context.

To test the hypothesis of the excess of soil humidity as force of selection favoring unsaturated fatty acids accumulation, studies with other tropical drought tolerant plant species are needed.

Table 2. Proportions of unsaturated fatty acids of *J. curcas* seed oils determinated by several authors in different parts of the tropical world.

Origin of the seeds	Unsaturated fatty acids (Percentage of the complete dry seed)	References
Malaysia	78.2*	Akbar et al. (2009)
Southern China	79.2±1.8	Wang et al. (2008)
Nigeria	61.9*	Adebowale and Adedire (2006)
Central Mexico	85.4±1.1	Martínez-Herrera et al. (2006)
Southeast Mexico	80.7±2.2	Ovando-Medina et al. (2011)

*Data of the Standard Deviation is not provided.

Conflict of Interest

The authors have not declared any conflict of interest.

REFERENCES

Adebowale KO, Adedire CO (2006). Chemical composition and insecticidal properties of the underutilized *Jatropha curcas* seed oil. Afr. J. Biotechnol. 5(10):901-906.

Aitzetmüller K, Tsevegsüren N, Werner G (1999). Seed oil fatty acid patterns of the Aconitum-Delphinium-Helleborus complex (Ranunculaceae). Plant Syst. Evol. 215:37-47.

Akbar E, Yaakob Z, Kamarudin SK, Ismail M, Salimon J (2009). Characteristic and composition of *Jatropha curcas* oil seed from Malaysia and its potential as biodiesel feedstock. Eur. J. Sci. Res. 29(3):396-403.

Arditti J (1967). Factors affecting the germination of orchid seeds. Bot. Rev. 33(1):1-97.

Arditti J, Ernst R (1984). Physiology of germinating orchid seeds. *In*: Arditti, J. (ed.). Orchid Biology: Reviews and perspectives III. Cornell University Press. Ithaca, U.S.A.

Barker GC, Larson TR, Graham IA, Lynn JR, King GJ (2007). Novel insights into seed fatty acid synthesis and modification pathways from genetic diversity and quantitative trait loci analysis of the *Brassica* C Genome. Plant Physiol. 144:1827-1842.

Bewley JD, Black M (1994). Seeds: Physiology of development and germination. Plenum Press. New York, U.S.A., pp. 1-31.

Bezard J, Bugaut M, Clement G (1971). Triglyceride composition of coconut oil. J. Am. Oil Chem. Soc. 48(3):134-139.

Canvin DT (1965). The effect of temperature on the oil content and fatty acid composition of the oils from several oil seed crops. Can. J. Bot. 43(1):63-69.

Coleman RA, Lee DP (2004). Enzymes of triacylglycerol synthesis and their regulation. Prog. Lipid Res. 43(2):134-176.

Dehgan B, Schutzman B (1994). Contributions toward a monograph of neotropical *Jatropha*: phenetic and phylogenetic analyses. Ann. Missouri Bot. Gard. 81:349-367.

Dehgan B, Webster G (1979). Morphology and infrageneric relationships of the genus *Jatropha* (Euphorbiaceae). Univ. Calif. Pub. Bot. 74:1-73.

Dyer JM, Chapital DC, Kuan JW, Mullen RT, Turner C, McKeon TA, Pepperman AB (2002). Molecular analysis of a bifunctional fatty acid conjugase/desaturase from Tung. Implications for the evolution of plant fatty acid diversity. Plant Physiol. 130:2027-2038.

Fairless D (2007). Biofuel: the little shrub that could maybe. Nature 449:652-655.

Gubitz GM, Mittelbach M, Trabi M (1999). Exploitation of the tropical oil seed plant Jatropha curcas L. Bioresour. Technol. 67(1):73-82.

Heller J (1996). Physic nut. *Jatropha curcas* L. Promoting the conservation and use of underutilized and neglected crops. 1. Institute of Plant Genetics and Crop Plant Research, Gatersleben/ International Plant Genetic Resources Institute. Rome.

Hosamani KM, Katagi KS (2008). Characterization and structure elucidation of 12-hydroxyoctadec-cis-9-enoic acid in *Jatropha gossypifolia* and *Hevea brasiliensis* seed oils: a rich source of hydroxy fatty acid. Chem. Phys. Lipids 152:9-12.

Ichie T, Ninomiya I, Ogino K (2001). Utilization of seed reserves during germination and early seedling growth by *Dryobalanops lanceolata* (Dipterocarpaceae). J. Trop. Ecol. 17(3):371-378.

Lersten NR, Czlapinski AR, Curtis JD, Freckmann R, Horner HT (2006). Oil bodies in leaf mesophyll cells of angiosperms: Overview and a selected survey. Am. J. Bot. 93(12):1731-1739.

Linder CR (2000). Adaptive Evolution of Seed Oils in Plants: Accounting for the Biogeographic Distribution of Saturated and Unsaturated Fatty Acids in Seed Oils. Am. Nat. 156:442-458.

Manning JC, Staden JV (1987). The development and mobilization of seed reserves in some African orchids. Austral. J. Bot. 35(3):343-353.

Musafarov DC, Mazhidov KK (1997). Chemical composition of husked and polished rice. Chem. Nat. Compounds 33(5):601-602.

Ovando-Medina I, Espinosa-García FJ, Núñez-Farfán J, Salvador-Figueroa M (2011). Genetic variation in Mexican *Jatropha curcas* L. estimated with seed oil fatty acids. J. Oleo Sci. 60(6):301-311.

Pramanik K (2003). Properties and use of *Jatropha curcas* oil and diesel fuel blens in compression ignition engine. Renew. Energ. 28(2):239-248.

Prutsch J, Schardt A, Schill R (2000). Adaptations of an orchid seed to water uptake and storage. Plant Syst. Evol. 220:69-75.

Pujar A, Jaiswal P, Kellog EA, Ilic K, Vincent L, Avraham S, Stevens P, Zapata F, Reiser L, Rhee SY, Sachs MM, Schaeffer M, Stein L, Ware D, McCouch S (2006). Whole-plant growth stage ontology for angiosperms and ist application in plant biology. Plan Physiol. 142:414-428.

Salvador-Figueroa M, Magaña-Ramos J, Vázquez-Ovando JA, Adriano-Anaya ML, Ovando-Medina I (2015). Genetic diversity and structure of *Jatropha curcas* L. in its centre of origin. Plant Genet. Resour. 13:9-17.

Sambanthamurthi R, Sundram K, Tan YA (2000). Chemistry and biochemistry of palm oil. Prog. Lipid Res. 39(6):507-558.

Sharma OP (1993). Plant taxonomy. Tata McGraw-Hill. New Delhi, India, pp. 95-101.

Smith CRJ (1970). Occurrence of unusual fatty acids in plants. Prog. Chem. Fats Other Lipids 11:139-177.

Vinogradova TN, Andronova EV (2002). Development of orchid seeds and seedlings. In: T. Kull and J. Arditti (eds.). Orchid Biology: Reviews and Perspectives VIII. Kluwer Academic Publishers. The Netherlands, pp. 167-234.

Voelker T, Kinney AJ (2001). Variations in the biosynthesis of seed-storage lipids. Ann. Rev. Plant Physiol. Plant Mol. Biol. 52:335-361.

Wang ZY, Lin JM, Xu ZF (2008). Oil contents and fatty acid composition in *Jatropha curcas* seeds collected from different regions. Nan Fang Yi Ke Da Xue Xue Bao (J. South. Med. Univ.) 28(6):1045-1046.

Westoby M, Jurado E, Leishman M (1992). Comparative evolutionary ecology of seed size. Trends Ecol. Evol. 7:368-372.

White JA, Todd J, Newman T, Focks N, Girke T, Martínez-de-Ilárduya O, Jaworski JG, Ohlrogge JB, Benning C (2000). A new set of *Arabidopsis* expressed sequence tags from developing seeds. The metabolic pathway from carbohydrates to seed oil. Plant Physiol. 124:1582-1594.

Woodworth CM, Leng ER, Jugenheimer RW (1952). Fifty generations of selection for protein and oil in corn. Agron. J. 44:60-65.

academicJournals

Vol. 10(17), pp. 549-558, 15 September, 2015
DOI: 10.5897/SRE2015.6264
Article Number: 5C00D7A46891
ISSN 1992-2248

http://www.academicjournals.org/SRE

Scientific Research and Essays

Full Length Research Paper

Identification of the damage model parameters of thrust ball bearings under variable operating regime

O. Djebili[1]* and F. Bolaers[2]

[1]Laboratory Dynamic of Motors and Vibroacoustics, UMBB Boumerdes, Algérie.
[2]Laboratory Grespi/LMA, UFR, Sciences Exactes et Naturelles Moulin de la Housse, BP 1039, 51687 Reims Cedex 2, France.

Received 24 May, 2015; Accepted 31 August, 2015

Bearing is an important component of a rotating machine; however, under normal operating conditions, it is subjected to fatigue which results in a defect called spalling. This work presents a monitoring fatigue of a thrust ball bearing on a bearing fatigue test bench. Spalling is artificially initiated on a bearing raceway. Vibration analysis is the method used to characterize the defect. The experimental procedure used is to monitor the operation of the ball bearing to the degradation with an online acquisition of the vibration readings. These data allow plotting the curve of fatigue (mathematical model). In order to obtain more realistic curve, the spalling evolution of several thrust ball bearings is monitored, first, under different loads then at different rotation speeds under a constant load. It found that growth follows a spalling power law and the damage is characterized by the model parameters.

Key words: Predictive maintenance, bearing, vibration analysis, spalling, rolling fatigue.

INTRODUCTION

The increased mechanization and automation of the rotating machines have made that the diagnosis is computerized and prognosis systems are a valuable tool in decision taking by maintenance personnel to intervene timely on equipment. Today, the concept of machinery diagnosis includes automatic detection and classification of defects, while the prognosis is a concept of predictive maintenance based mainly on estimating the likely time remaining before the failure occurs on a machine. Predicting failures promises to significantly reduce maintenance costs such as machine stops, consumption of spare parts, etc. However, it still remains an axis of current research and is a major concern of researchers in the maintenance field. Among approaches about predictive maintenance reported in the literature, it distinguished Pusey and Roemer (1999) who gave an overview of the development of diagnosis and prognosis for high technological performance applicable on turbomachinery until 1999. Jardine et al. (2006) gave an overview and publications on acquisition and processing of data, diagnosis and prognosis of various machines until 2005. Basile (2007) developed a statistical approach to establish a law for equipment reliability; this approach is based on the feedback (time base failures included). Vachtsevanos et al. (2006) identified and described fault diagnosis by artificial intelligence methods and approaches

*Corresponding author. E-mail: omar_djebili@yahoo.com

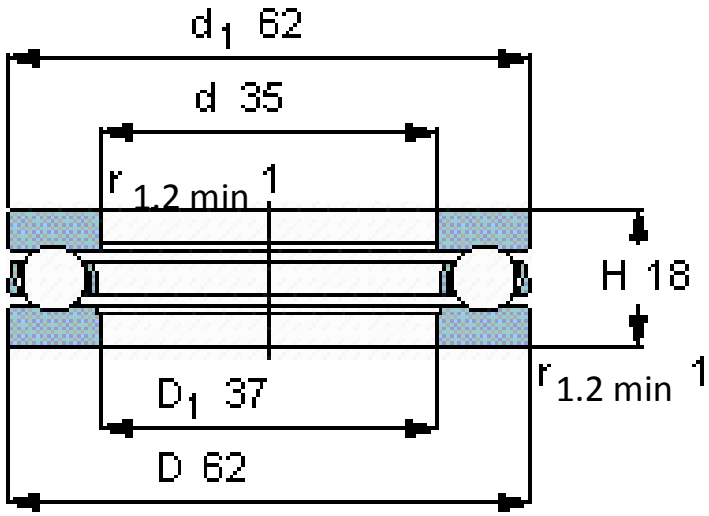

Figure 1. Thrust ball bearing.

to the prediction of failures in engineering systems through examples.

This research consists, firstly to show whether the model of thrust ball bearing fatigue obtained during our previous work is still valid in case operating conditions of the machine change, then to confirm the identification and the significance of the degradation model parameters (Djebili, 2013; Djebili et al., 2013). The occurrence of spalling at a point of contact between the rolling elements and bearing raceway is a random phenomenon whose probability of occurrence is related to the combination:

(i) Between the stress level and the probability of finding a more or less harmful inclusion for chipping, initiated into sub-layers;
(ii) Between the stress level and the probability of finding a surface defect for chipping insiders' surface.

To save time and to control the position of occurrence of spalling, an artificial defect is created using a graphite tool having a piece of rounded shape with a diameter 2 mm at a fixed point of the ball trajectory on the bearing ring. This artificial indentation is formed on an electrical discharge machine and used to initiate a spalling fault by creating a stress concentration. Monitoring the evolution of spalling is then performed in change of machine operating conditions (test bench of bearing fatigue) by successively varying the following parameters:

(i) Axial load applied on the thrust ball bearing,
(ii) Rotation speed of the thrust ball bearing axis.

Then, it will be possible, from the knowledge of loading conditions (corresponding pressure) and operating conditions (rotating speed) to predict the evolution of a thrust ball bearing spalling using the fatigue model with more reliability.

VIBRATION MONITORING OF A THRUST BALL BEARING SUBJECTED TO DIFFERENT LOADS

Description of the thrust bearing

Bearings (Figure 1) mounted on the module are thrust bearings whose characteristics are: FAG 51207 CZECH / ATK, inner diameter di_1= 35 mm, di_2 = 37 mm, outer diameter D = 62 mm, number of balls N_b = 12.

Test procedure

Before initiating a defect on the mobile ring of the thrust ball bearing, it is required to turn the bearing on the fatigue test bench (Figure 2) during an operating lifetime defined by the L_{10} probability (Alfredson and Mathew, 1985). Concerning tests, it used different axial loads on the bearings and L_{10} lifetimes (ISO 281, 2007) are shown in Table 1.

After each L_{10} lifetime to a given axial load, it proceeds to removal of the thrust ball bearing and to initiate a defect on one of the rings (Figures 3 and 4). Then it put back the bearing on the test bench to rotate during the spalling phase. The tests are performed on a test bench on which it sets value of the axial load to transmit at the thrust ball bearing, constant rotation speed of 1800 RPM and flow of cooling liquid. Two piezoelectric accelerometers type DJB3208 and DJB3209 are placed near the bearing in two different directions (axial and radial) to acquire the vibration signals.

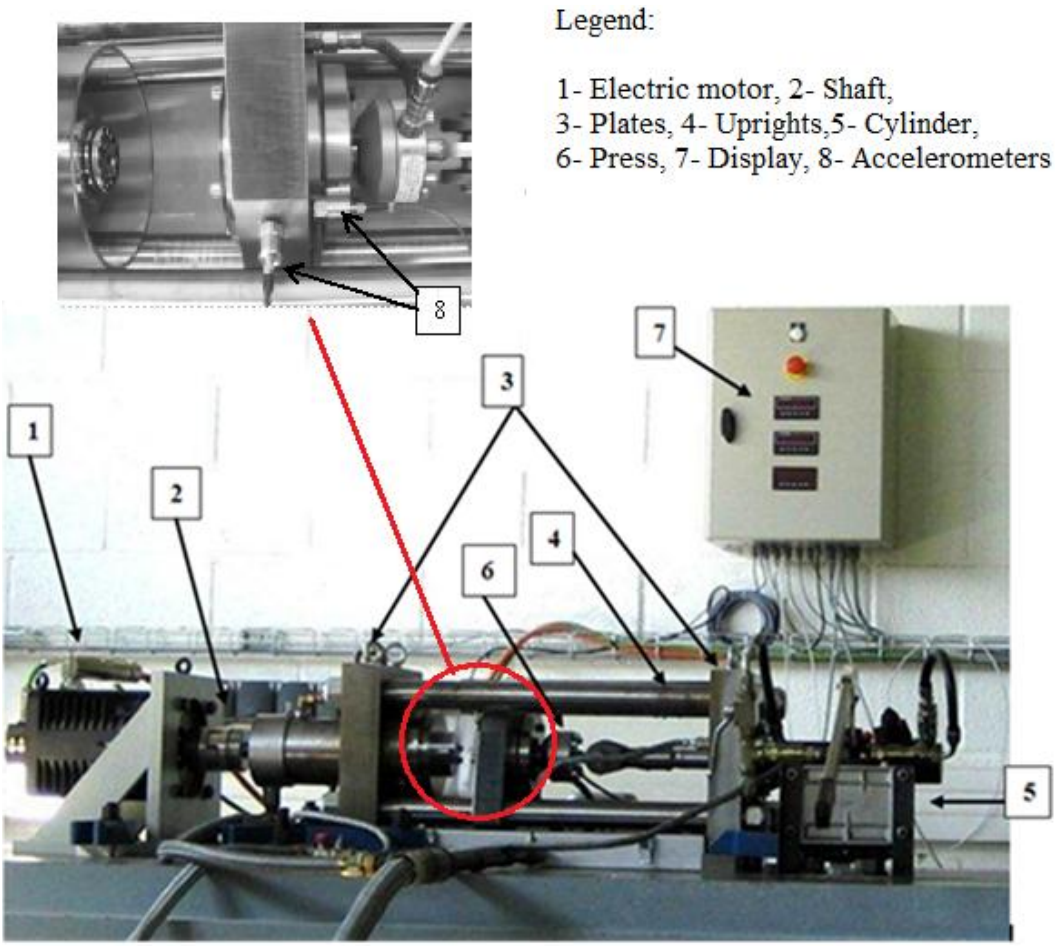

Figure 2. Test bench of the thrust ball bearing fatigue.

Table 1. Bearing lifetimes.

Axial load(N)	Rotation speed (RPM)	Life time L_{10} (h)
30000	1800	$L_{10(1)}$=25
35000	1800	$L_{10(2)}$=13
40000	1800	$L_{10(3)}$=9

These are connected to the installation in order to indicate the vibration level instantly.

This test bench consists of three main parts: (i) base which is consists of two plates (3) linked with four uprights (4); (ii) the training part, including the main shaft (2) which goes through a plate to allow positioning of the thrust bearing to be tested on one of its end and the electric motor (1) which transmits the rotation movement to the shaft by means of a coupling; (iii) the load device support, including the cylinder (5) which loads the press (6), the intensity of the load is indicated by a display (7). The defect size is measured periodically to readjust the model (Figure 5). These measurements are performed using a microscope with a camera and software that quantifies the spalling size.

Evolution of the defect size

Monitoring of the spalling evolution is realized with several thrust ball bearings on the test bench fatigue subjected to variable loads and a constant rotation speed. Figure 6 shows the evolution of the obtained spalling curves.

It is found that spalling growth follows the power law of type $f(x) = a.x^b$ (Richalet, 1998) and depends on the load.

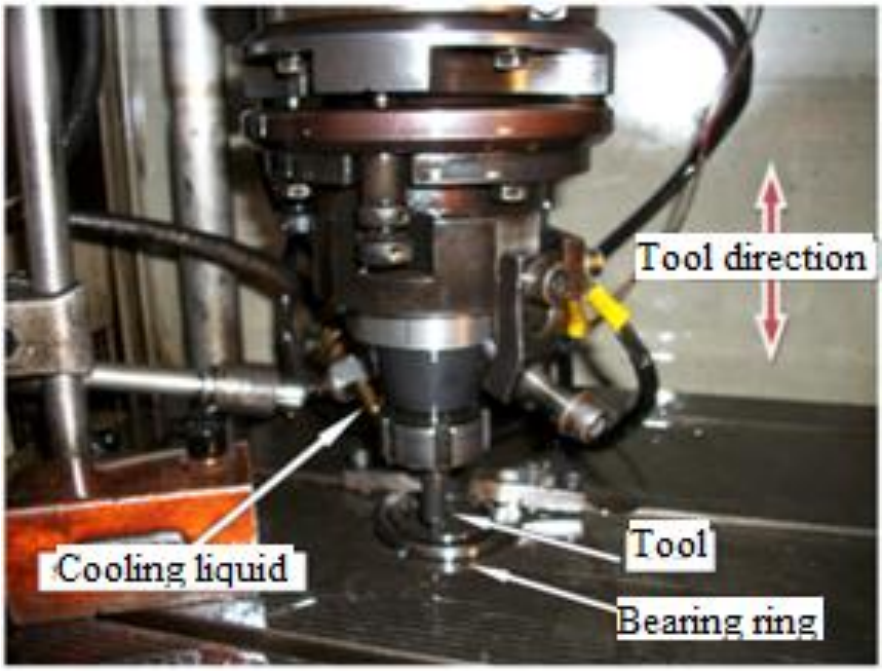

Figure 3. Booting the defect on the bearing ring using the sinking EDM machine.

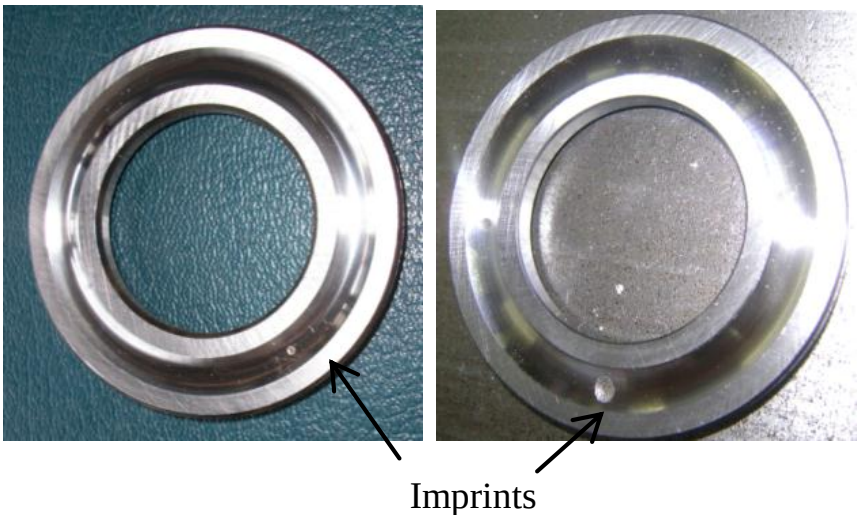

Figure 4. Spalling defect on a thrust ball bearing.

Calculation of Hertz pressure

It uses the formula concerning the Hertz contact between two solids to calculate the Hertz pressure generated between the ball and the ring of the thrust ball bearing.

$$P_{max} = \frac{3N}{2\pi kl} \quad (1)$$

The materials of the ball and the ring are identical. The contact surface generated is elliptical shape with large semi -axis k and small semi-axis l. N = Q/12: axial load applied to each bearing ball. For full load Q = 30000 N, the maximum pressure is: P = 3.3 GPa (Table 2).

Experimental results

The power law coefficient ‘a’ grows with increasing load and the spalling time decreases with increasing load

Figure 5. Measurement of the spalling fault size.

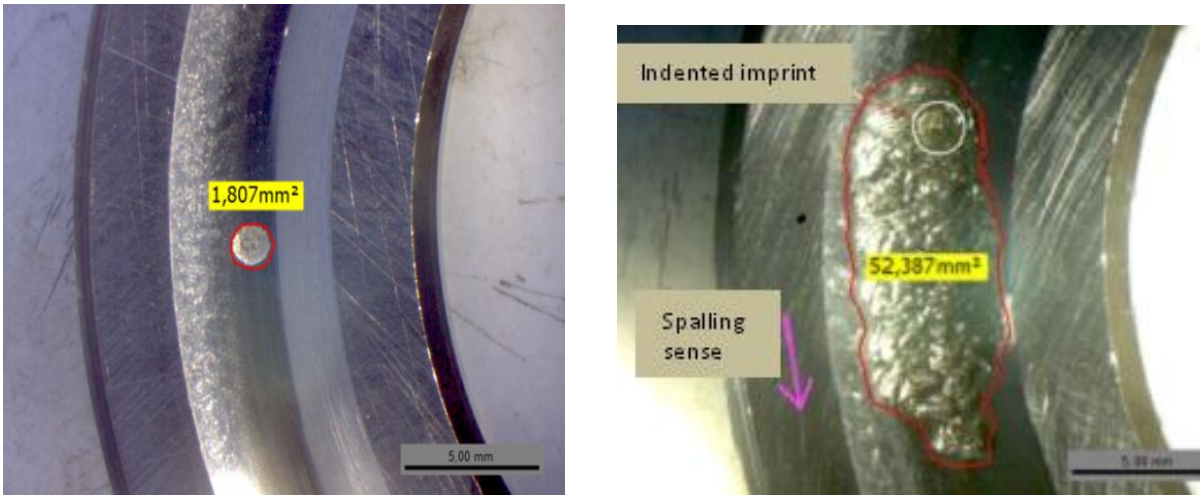

(a) (b)

Figure 6. Evolution of spalling on a thrust ball bearing ring, (a): Initiated fault, (b): Spalling fault.

during the spalling phase (until fault area threshold 48 to 52 mm^2) (Figure 7).

Evolution of the vibration indicator

We proceed in the same way to monitor the vibration indicator over time. Monitoring of the spalling evolution is realized on several thrust ball bearings under continuous operation and subjected to varying loads. Measurements are taken on the test bench in a wide range of acquisition frequency (0 - 20 kHz). It is to define the band of frequencies (f1, f2) in which a vibration energy is maximum (Li et al., 2000). This energy corresponds to

Table 2. Cycles number of spalling phase.

Axial load (N)	Hertz pressure (Gpa)	Spalling cycles number
30000	3.3	N_1=468000
35000	3.48	N_2=288000
40000	3.61	N_3=180000

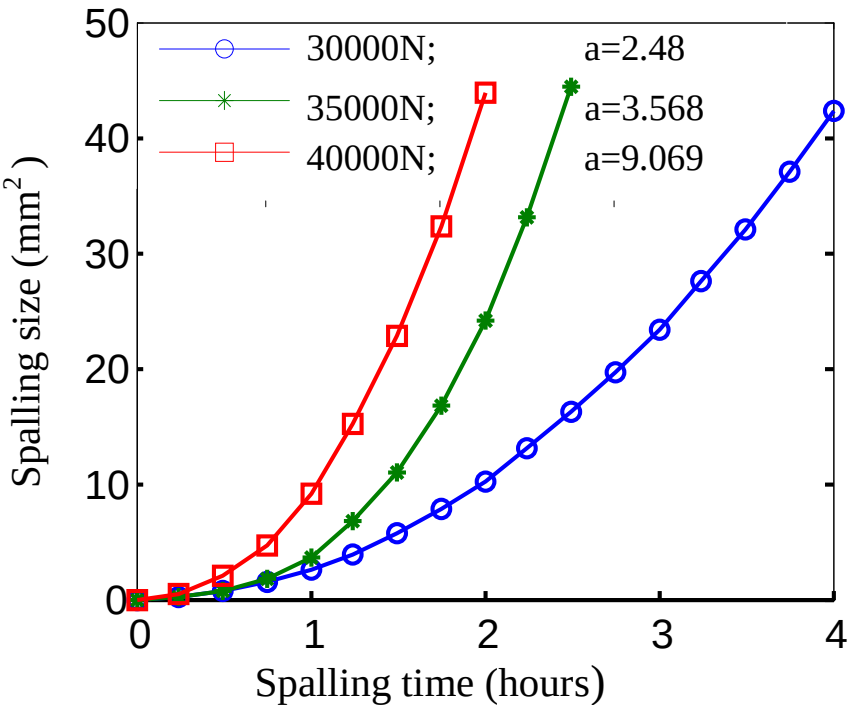

Figure 7. Evolution curves of spalling size at different loadings.

the structure resonances generated by a bearing fault. These resonances are typically between 10000Hz and 15000Hz in case of rotating machines (Djebili et al., 2013). Figure 8 shows spalling evolution curves of three thrust bearings at a constant speed. It finds that spalling growth follows the power law of type f (x) = a.x^b and depends on the load. The spalling of bearings grows with different cycle numbers N1, N2 and N3 according to the applied pressure. These results are presented in Table 3.

In Tables 2 and 3, the cycle number define for both cases, the duration of the spalling phase just shows increase with decreasing load. The evolution of the thrust ball bearing spalling follows a power law model, therefore confirms the results of previous tests and the coefficient 'a' of the power law increases with increasing of the load according to Table 4.

Discussion of results

According to the obtained results from the fatigue tests on thrust ball bearings, the statistical indicator of spalling fault evolves with applied axial load on the bearings. Figure 9 shows three curves representing the variation of the RMS indicator values according to the pressure on the bearing. Through these curves, the RMS values of the statistical indicator grow rapidly with increasing of the axial load on the thrust ball bearing and the points of curves diverge increasingly further. In fact, the differences between the points of the curves relating to load 40000 N are greater than the differences between the points of the curves relating to load 35000 N and further larger than those between the points of the curves relating to load 30000 N. It can conclude and confirm that more load is important during the thrust ball bearing operation, the spalling increase is relatively fast.

ROTATION SPEED VARIATION OF THE THRUST BALL BEARING

It acts on the variation of a second parameter of the

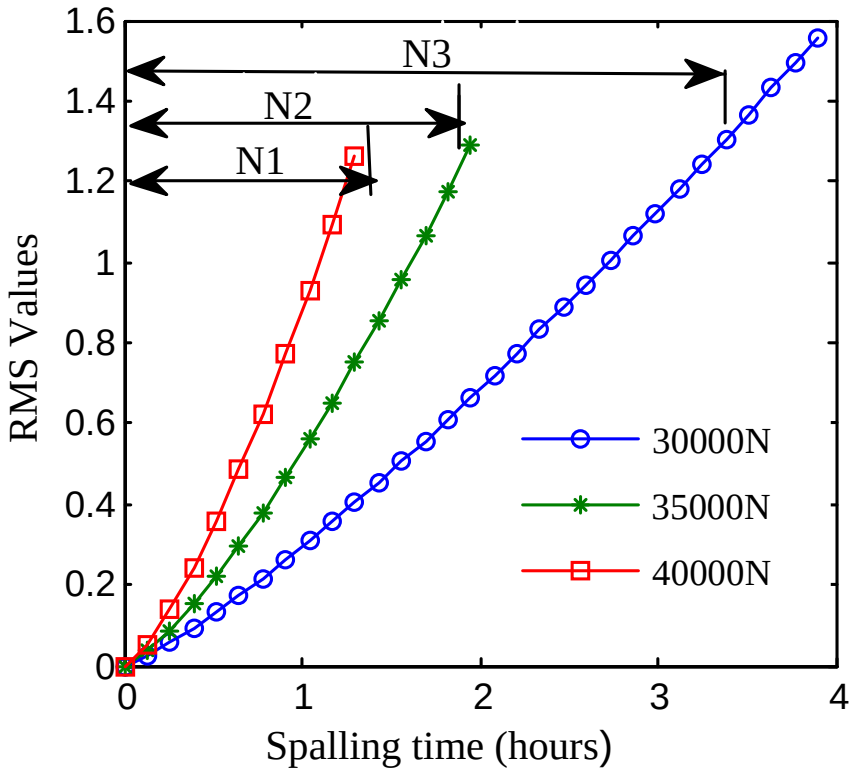

Figure 8. Evolution curves of the root mean square (RMS) indicator (Hoeprich, 1992) at different loads.

Table 3. Cycle numbers of spalling phase.

Axial load (N)	Hertz pressure (Gpa)	Spalling cycles number
30000	3.3	N1=369000
35000	3.48	N2=225000
40000	3.61	N3=108000

Table 4. Values of the power law coefficients.

Axial load (N)	Coefficient (a)	Coefficient (b)
30000	0.292	1.23
35000	0.53	1.33
40000	0.885	1.38

operating conditions of the machine which is the rotation speed of the thrust ball bearing to see its effect on the fatigue model. For this purpose, other fatigue tests are made again on thrust ball bearings. They consist of:

(i) Initiating the fault on one of the bearing rings,
(ii) Applying the same constant load on bearings,
(iii) Varying the rotation speed of bearings,
(iv) Operating the bearings continuously on the test bench until degradation.

Damage curves evolution

Monitoring the evolution of damage is then performed under a constant load of 30000 N. T1, T2 and T3

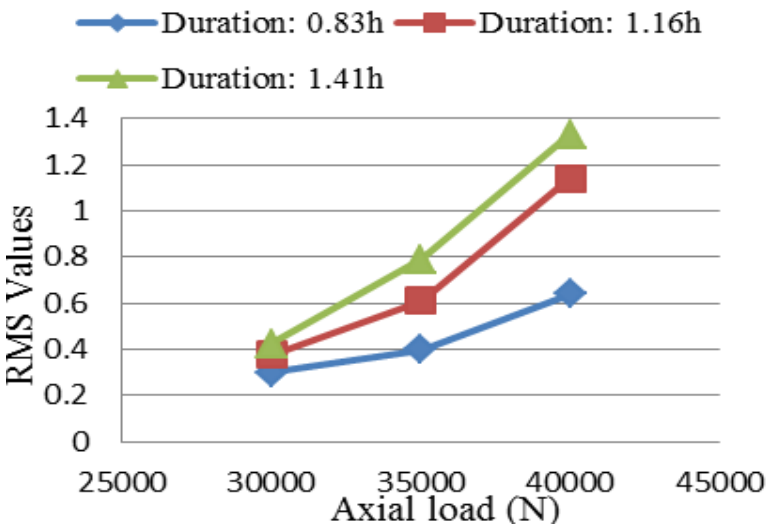

Figure 9. Vibration amplitude according to the axial load during the spalling phase.

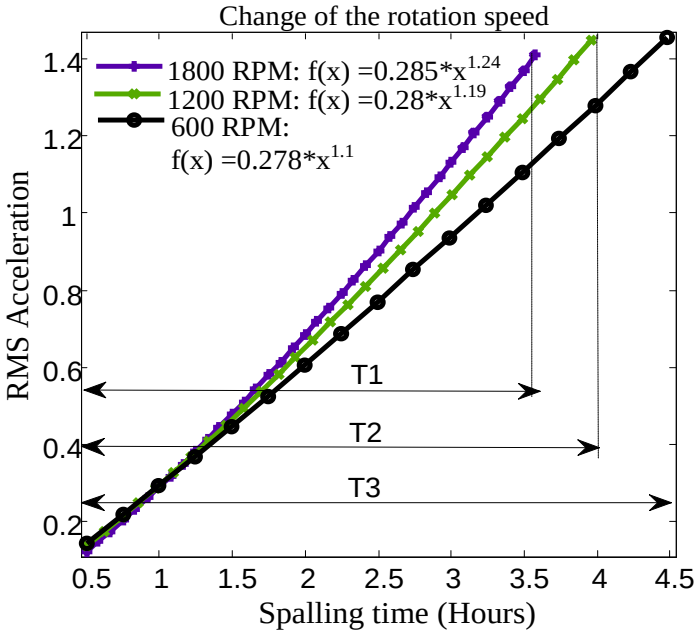

Figure 10. Comparison of evolution curves according to different rotation speed.

(Figure 10) are spalling phase's durations of thrust ball bearings respectively to rotation speed 1800 RPM, 1200 RPM and 600 RPM.

Discussion of results

Through the damage curves evolution obtained in Figure 10, it is noted that the coefficient value b of the power law on Table 5 increases with increasing of the rotation speed of the thrust ball bearing.

The damage curves analysis concluded that more rotation speed is high, the spalling phase duration is reduced and the coefficient value b is large. These results show that the thrust ball bearing damage is characterized by the coefficient b. Three curves are plotted in Figure 10 to represent the evolution of the RMS indicator values with respect to the rotation speed.

Regarding curves on Figure 11, the RMS values of the statistical indicator grow with rotation speed increase of

Table 5. Coefficients values of the power law.

Rotation Speed (RPM)	Coefficient (a)	Coefficient (b)
600	0.278	1.1
1200	0.28	1.19
1800	0.285	1.24

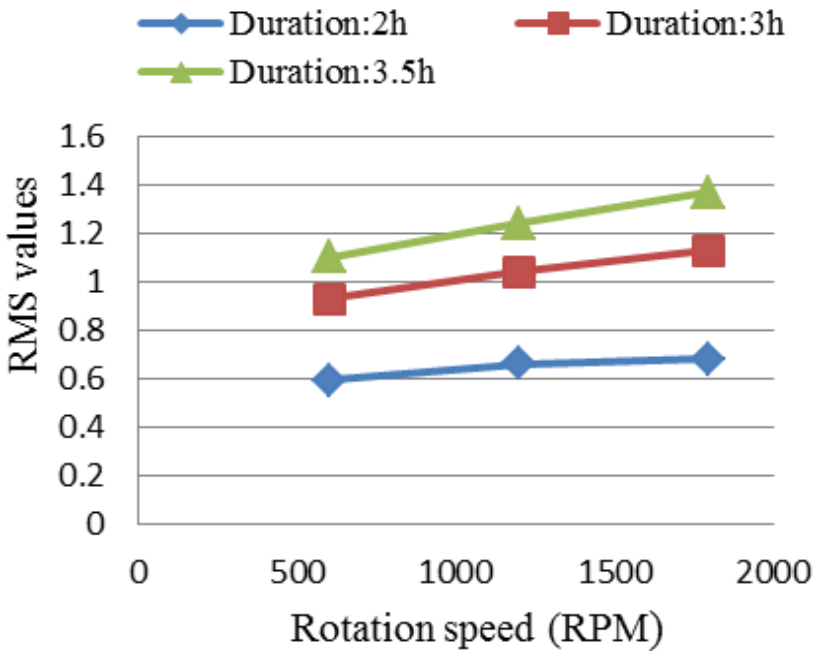

Figure 11. Vibration amplitude according to the rotation speed during a spalling phase.

the thrust ball bearing and the points of curves diverge increasingly from the small to the large speed but not with the same importance as those of curves representing the indicator evolution according to the load.

It can also confirm that more rotation speed is important, the increased spalling is relatively significant. In fact, the differences between the curves points relating to load 40000 N are greater than the differences between the curves points relating to load 35000 N and further larger than those between the curves points relating to load 30000 N. Fatigue tests on the thrust ball bearings subjected to a change in the operating conditions of the test bench have shown that the increased spalling under increasing axial load is more important than increased spalling under increasing rotation speed.

CHARACTERIZATION OF THE DAMAGE LAW PARAMETERS

The experimental results have identified the damage law parameters concerning a spalling phase. This law is a power function (Li et al., 1999):

$$D = aN^b \quad (2)$$

Where D: damage at time t_i to the pressure P and the rotation speed n, N: operating time or number of cycles at time t_i, a: empirical parameter depending on the load, b: empirical parameter depending on the rotation speed of the thrust ball bearing.

Therefore, monitoring the evolution in time of a vibration indicator allows establishing a trend curve (Williams et al., 2001; Li et al., 2000). From the above results, a and b parameters (coefficients) values are determined by the least squares method applied to each vibration reading using a Matlab program (Richalet, 1998; Adrian and Moshe, Version 6 and 7). The results of various tests have also shown that law coefficients of the spalling growth vary with change of the applied axial load and the rotation speed of the thrust ball bearing. The type of power damage model seems to characterize the thrust ball bearings degradation. This spalling growth model is a

phenomenological model obtained by a physical approach with experimental identified parameters using vibration analysis method (Alfredson and Mathew, 1985; Alfredson and Mathew, 1985; Djebili et al., 2013). Therefore the spalling growth is subjected by determination of **a** and **b** coefficients which characterize respectively the Hertz pressure and damage (Djebili, 2013).

CONCLUSION AND PERSPECTIVES

This research is focused on vibratory monitoring of the spalling initiated on thrust ball bearings with operating conditions change. The vibration analysis method is used to determine the growth model parameters of the spalling phase using vibration measurements and identify those parameters through the obtained results. Fatigue tests have shown that coefficients of the bearing fatigue model grow with increasing load and rotation speed values concerning the test bench operating regime. Through these results, change in parameters related to the operating conditions of the machine showed clearly the interpretation of the coefficients **a** and **b** of the fatigue model. They respectively characterize the Hertz pressure and damage. As the final objective of the work is to determine the remaining life defined as the fatigue cycles number to achieve a spalling area (in the case of thrust ball bearings tested ≈ 50 mm^2), so it is possible to estimate from modeling the spalling growth. Use of the damage model whose parameters are determined for the actual operating conditions data may be more interesting to predict failure. Therefore, from loading and operation conditions of thrust ball bearings, it is possible to further estimate the spalling growth law and predicts the evolution of damage and duration corresponding remaining lifetime knowing the threshold fault (must not be exceeded).

The work done until now still needs more efforts to improve the growth model of thrust ball bearing fatigue. The improved model is to consider other parameters that can affect the bearing fatigue during running time such as temperature. Our wish is to build abacuses for fatigue model to then be used for:

(i) All operating conditions of the machine,
(ii) State of the environment (local, outside, etc.) of the machine.

The exploitation of these abacuses will be more convenient by maintenance users to ensure quality and optimal maintenance.

Conflict of Interest

The authors have not declared any conflict of interest.

REFERENCES

Adrian B, Moshe B (Version 6 and 7). Matlab pour l'ingénieur.
Alfredson RJ, Mathew J (1985). Frequency domain methods for monitoring the condition of rolling element bearings. Mech. Eng. Trans,--Inst. Eng. Aust. 2:102-107.
Alfredson RJ, Mathew J (1985). Time domain methods for monitoring the condition of rolling element bearings. Mech. Eng. Trans,--Inst. Eng. Aust. 2:108-112.
Basile O (2007). Prise en compte de l'incertitude dans les modèles fiabilistes industriels, Extensions aux sollicitations variables. Doctoral thesis, Faculté Polytechnique de Mons.
Djebili O (2013). Contribution à la maintenance prédictive par analyse vibratoire des composants mécaniques tournants, application aux butées à billes soumises à la fatigue de contact de roulement. Doctoral thesis.
Djebili O, Bolaers F, Laggoun A, Dron JP (2013). Follow up of the growth of a rolling fatigue spalling within a predictive maintenance. J. Mech. Ind. 14:85-93.
Djebili O, Laggoun A, Bolaers F, Dron JP (2013). Methodological approach of selecting a vibration indicator in monitoring bearings. Int. J. Phys. Sci. 8 (12):451-458.
Hoeprich MR (1992). Rolling Element Bearing Fatigue Damage Propagation. J. Tribol. 114(2):328-333.
Jardine AK, Lin D, Banjevic D (2006). A review on machinery diagnostics and prognostics implementing condition-based maintenance. J. Mech. Syst. Signal Process. 20:1483-1510.
Li Y, Billington S, Zhang C, Kurfess T, Danyluk S, Liang S (1999). « Adaptive prognostics for rolling element bearing condition ». J. Mech. Syst. Signal Process. 13(1):103-113.
Li Y, Kurfess TR, Liang SY (2000). Stochastic prognostics for rolling elements bearings. J. Mech. Syst. Signal Process. 14(5):747-762.
Norme ISO 281 (2007). Roulements - Charges dynamiques de base et durée nominale.
Pusey HC, Roemer MJ (1999). An assessment of turbomachinery condition monitoring and failure prognosis technology. The Shock and Vibration Digest 31:365-371.
Richalet J (1998). Pratique de l'identification. Hermes Sciences Publications.
Vachtsevanos G, Lewis FL, Roemer M, Hess A, Wu B (2006). Intelligent fault diagnosis and prognosis for engineering systems. John Wiley & Sons, Inc. Hoboken. ISBN: 978-0-471-72999-0.
Williams T, Ribadeneira X, Billington S, Kurfess T (2001). Rolling element bearing diagnostics in run-to-failure lifetime testing. J. Mech. Syst. Signal Process. 15(5):979-93.

academicJournals

Vol. 10(17), pp. xxx-xxx, 15 September, 2015
DOI: 10.5897/SRE2015.6317
Article Number:xxxxxx
ISSN 1992-2248

http://www.academicjournals.org/SRE

Scientific Research and Essays

Full Length Research Paper

Predicting the permeability of pervious concrete pavement using artificial neural networks modeling

Hassan Tajik Ghashghaei and Abolfazl Hassani*

Department of Civil Engineering and Environment, Tarbiat Modares University, Tehran, Iran.

Received 15 August, 2015; Accepted 2 September, 2015

Pervious concrete (PC) pavement is a sustainable type of concrete pavement that can protect and restore natural ecosystem. The permeability coefficient is the most important characteristic of PC. The purpose of this experimental study was to investigate the effect of mixture design parameters, particularly water-to-cement ratio (W/C) and size of aggregate on the permeability coefficient of PC. The thirty six mixtures were made with W/C in range of 0.28 to 0.34, 350 kg/m^3 cement content and 9.5 to 19.5 mm maximum size of aggregate. In this study the feasibility of using the artificial neural networks (ANN) in predicting the effect of aggregate size and W/C on amount of permeability coefficient of PC was investigated. For modeling, 65% of data was used for model training and remaining 35% was used for model testing. Based on the lowest root mean squared error (RMSE), the best ANN model was chosen. The results showed that the W/C and aggregate size are key parameter, which significantly affect the performance of PC. The ANN modeling was developed in this study can facilitate prediction permeability coefficient of PC. This approach can reduce the number of trial batches for target performance of samples.

Key words: Pervious concrete, artificial neural network, permeability coefficient.

INTRODUCTION

Pervious concrete (PC) is a special type of concrete characterized by an interconnected pore structure and high void content, thus allowing infiltration of water through its structure. While its constituent materials are similar to that of normal concrete, PC contains little or no fine aggregate. It is also known as permeable concrete, porous concrete and no-fine concrete. PC has been used in low-traffic pavements such as parking lots and sidewalks (Schaefer et al., 2006). Permeability coefficient or hydraulic conductivity is the most important performance characteristic of PCs, and with any some material, transportation property are dependent on the pore structure features (Montes and Haselbach, 2006). The PC allows water to pass through its structure due to an increased air voids network. This open structure gives this concrete the added possibility to be applied in pavement engineering as a water drainage layer (Vassilikou et at., 2011). The costs of such asphalt pavements will grow the coming years due to the foreseeable increase in oil prices. PC is therefore a suitable material to be considered for increased usage in the developing sustainable pavement (Lian and Zhuge,

*Corresponding author. E-mail: hassani@modares.ac.ir

Table 1. Engineering properties of aggregates.

Flakiness Index (%) (BS-812)	Water absorption (%) (AASHTO T-85)	Los Angeles abrasion (%) (AASHTO T-96)	Sand equivalent (%) (AASHTO T-176)
10	3	13	70

Table 2. The Chemical properties of cement Type 2, according to ASTM C150 (Tehran Cement Co. Specification).

Constituent compounds	CaO, %	SiO_2, %	Al_2O_3, %	Fe_2O_3, %	MgO, %	SO_3, %	L.O.I, %	I.R, %
Measured value	63.35	21.45	4.61	3.3	2.26	2.05	2.00	0.57

2010; Vancura, 2011; Sumanasooriya and Neithalath, 2011). Natural resources are increasingly consumed due to rapid urbanization and there after human construction activities, so that various strategies are being investigated by engineers to protect and restore natural ecosystems in the world. PC pavement is termed as comprising material that facilitate storm water infiltrate and transfer to the underlying subsoil (Suozzo and Dewoolkar, 2012; Shu et al., 2011).

The porosity is the ratio of the volume of voids to the total volume of the specimen. Some of the voids in PC are not effective in carrying water through the material. The voids, which are frequently called the 'effective voids' are important. Some methods for finding the porosity of PC only calculate the effective voids (Boyer et al., 2012; Shen et al., 2012; Tho-in et al., 2012). Some researchers recommends to finding the total porosity of PC using a water displacement method. The water displacement method is based on Archimedes principle of buoyancy, which states that the buoyancy force is equal to the weight of fluids displaced. In this method, the dry mass, submerged mass and the total volume must be known to calculate the porosity (Montes et al., 2005).

Since the permeability coefficient of PC is the most important characteristic of PC, in this experimental study, the characteristic of PC has been evaluated. It's believed that PC can effectively assist solving drainage problems and reducing the risk of flash flooding, resulting from continuous urban development. The most important mixture design parameters for PC that affect the performance and workability are aggregate size and water-to-cement ratio (W/C). PC made with different W/C has different permeability coefficient. In this study an ANN modeling approach was used to determine the effect of aggregate size and W/C on permeability coefficient of PC.

EXPERIMENTAL PROGRAM

Materials and mixtures

A total of thirty-six PC samples were prepared and tested to determine the porosity content and permeability coefficient. The compositions used to prepare PC samples in this study consisted aggregates, ordinary Portland cement, and water.

All mixtures were designed with single size of crushed silica aggregates. The single size of aggregate defined as the size of sieve on which, 100% of aggregate was passed but all retained the sieve under that. Crushed silica aggregates with a size of 4.75-9.5, 9.5-12.5 and 12.5-19.5 mm were used in this study. Aggregates with a size of 4.75-9.5 mm were named fine and aggregates with a size of 9.5-12.5 mm were named medium and aggregates with a size of 12.5-19.5 mm were named coarse. Using single size aggregates for making samples, leads to gain higher porosity content. However, this approach reduces the workability of samples. The used aggregates were from the eastern area of Tehran. Three groups of samples for this study were developed. The first group was produced with only coarse aggregates with one grading (12.5-19.5 mm). The second group was produced with medium aggregates with one grading (9.5-12.5 mm). The third group was produced with fine aggregates with one grading (4.75-9.5 mm). The engineering properties of used aggregates are shown in Table 1.

For preparing all the PC mixtures, type 2 Portland cement was used. The chemical properties of used cement are shown in Table 2. The physical properties of used cement are shown in Table 3. All mixtures were produced by using single size aggregate and Portland cement with W/C of 0.28, 0.3, 0.32, and 0.34. 1400 kg of aggregates was used for making one cubic meter of PC mixes. The cement content of all the mixtures was around 350 kg/m^3. The W/C was incrementally changed from 0.28 to 0.34. In this way, samples of different porosity were obtained. PC mixes were made from fine aggregates was named Fine PC (FPC), PC mixes were made from medium aggregates was named Medium PC (MPC), and PC mixes were made from coarse aggregates was named Coarse PC (CPC). This division was used to compare the performance of PC mixes made from different aggregates size.

For making samples, materials were mixed in a rotating-drum mixer. For each mixture, triplicates of 100 × 200 mm cylinders were prepared. The fresh concrete was compacted in molds in three layers same to the one described in ASTM C 192; *Practice for making and curing concrete test specimens in the laboratory*. Instead of mechanical vibration because of the risk of blockage of the PC open pore structure, each layer tamped 15 times using a standard compacting bar. Excess concrete above the upper edge of the mold, was removed and a steel trowel was used to press on the surface for levelling. All specimens were de-molded after 24 h and stored in the curing room at 95% relative humidity.

Density test was performed for hardened concrete samples by simple dimensional checks, followed by weighting and calculation. The average density was 1800 kg/m^3 with a porosity of 37%. Picture of sample for permeability coefficient test is shown in Figure 1.

Table 3. The physical properties of cement type 2, according to ASTM C150 (Tehran Cement Co. Specification).

	Chemical properties			Blaine specific surface, cm^2/g	Autoclave expansion, %	Physical properties Setting time		Compressive strength MPa		
	Mg O%	L.O. I%	I.R %			Initial minutes	Final hours	3-day	At least 7 days	At last 28 days
Value	<6	<3	<0.75	>2800	<0.8	>45	<6	>10	>17	>21

Figure 1. PC Sample for permeability coefficient test.

Testing procedure

Permeability test

The permeability coefficient test was measured using the falling head method. Permeability coefficient was calculated using the Darcy's law as gives:

$$k = (A_1 l)/(A_2 t)\log(h_1/h_2) \quad (1)$$

Where A_1 and A_2 are the cross-sectional areas of the sample and the tube respectively, and L is the length of the specimen for typical specimen geometry, h_1 or h_2 are the initial and final heads of water and t is the time between transition water from h_1 to h_2. Picture of permeability coefficient test kit is shown in Figure 2.

The specimens were enclosed in a mold that was lined with a thin rubber sheet, and tightened with house clamps to minimize any flow along the sides of the mold that would affect the measurement of permeability coefficient. The sample was then connected to a vertical PVC pipe on both the upstream and downstream sides.

The apparatus was filled with water from the downstream end, to expel any air voids that may have been present in the PC sample. Once water head reached the top of the specimen, the apparatus was then filled from the upstream side. The system was allowed to reach equilibrium, at which time the water level was recorded, representing the head level on the downstream side. Maintaining the constant downstream head at a higher elevation than top of the PC sample provided full saturation throughout the test. The upstream water level was then increased to a height of 30 cm and the valve closed. The valve was then opened and water allowed to fall to a height of 10 cm, during which the time it look for the water level to fall was recorded. This head difference was expected to maintain laminar flow for the range of anticipated permeability coefficient.

Porosity test

The total porosity was measured by finding the difference of the PC sample cylinder weight submerged in the water and the weight after air drying for 24 h. The difference in the measured weights was then divided by the sample volume (mm^3) as follow (Park and Tia, 2004):

$$p = 1 - (((w_1 - w_2)/\rho_w)/v) * 100 \quad (2)$$

Where p is the total porosity of the PC (%), w_1 is the PC sample weight air-dried for 24 h (kg), w_2 is the PC sample weight submerged under water (kg), v is the PC sample volume (mm^3), and ρ_w is density of water (kg/mm^3).

Artificial neural networks

ANNs are data processing systems consisting of a large number of simple, highly interconnected processing elements (artificial neurons) in an architecture inspired by structure of the central cortex of the brain (Hola and Schabowicz, 2005; Mansour et al., 2004). Much of success of neural network is due to such characteristic as nonlinear processing and parallel processing. Neural networks model techniques have been rapidly applied in engineering, business, psychology, science, and medicine in recent years. In civil engineering the methodology of neural networks has been successfully applied to a number of areas such as structural analysis and design (Hajela and Berke, 1991; Consolazio, 2000).

In this study for ANN modeling, the multilayer perception (MLP) is

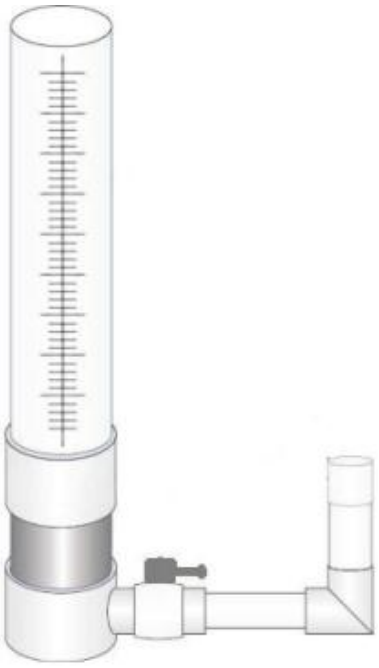

Figure 2. Falling head method kit for permeability coefficient measurement.

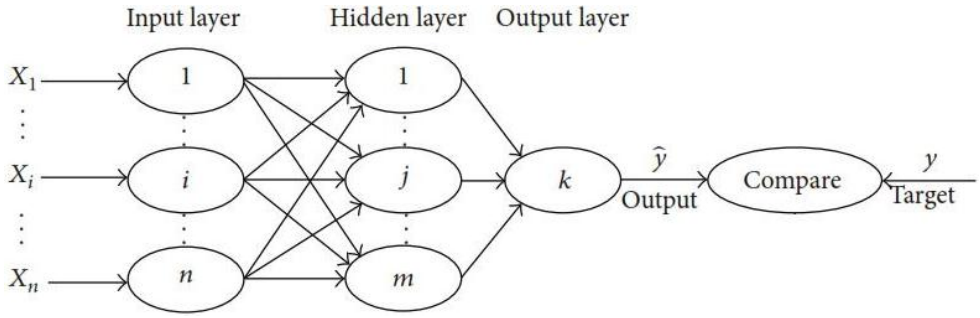

Figure 3. General framework of three-layered neural networks.

used. MLP is a feed forward artificial neural network model. MLP consists of multiple layers of nodes in a directed graph, with each layer fully connected to the next one. Three-layered ANN shown in Figure 3 was used in this study.

Three-layered feed forward neural networks (FFNN) are based on a linear combination of the input variables, which are transformed by a nonlinear activation function. The explicit expression for an output value of ANN is given by following equation:

$$y_k = f_o\left(\sum_{j=1}^{m} w_{kj}.f_h.\left(\sum_{i=1}^{n} w_{ji}.x_i + w_{jo}\right) + w_{ko}\right) \quad (3)$$

Where w_{ji} is the weight in the hidden layer connecting the ith neuron in the input layer and jth neuron in the hidden layer; w_{jo} is the bias for jth hidden neuron; f_h is the activation function of the hidden neuron; w_{kj} is the weight in the output layer connecting the jth neuron in the hidden layer and the kth neuron in the output layer; w_{ko} is the bias for the kth output neuron; f_o is the activation function for the output neuron. The weights are different in the hidden and output layer, and their values can be changed during the process of network.

To examine how close the predicted data to the experimental ones, some different criteria are used. There are two types of graphical and statistical criteria goodness of fit where each has its own unique features, and is used for a specific purpose. Since the graphical method is not accurate and varies depending on opinion of individual person, the statistical criteria were used in this study. Root mean square error (RMSE) is the most widely used statistical criteria. Finally, the best model, based on the lowest root mean square error coefficient, is chosen;

$$\mathrm{RMSE} = \left(\frac{1}{n}\sum_{i=1}^{n} (x_s - x_e)^2\right)^{0.5} \quad (4)$$

Where n is the number of data, x_e is experimental data, and x_s is

Table 4. All PC mixes measured properties.

PC mixtures	Size of aggregates (mm)	W/C	Porosity	Permeability coefficient (mm/s)
FPC1	9.5	0.28	0.390	11.3
FPC2	9.5	0.30	0.386	10.5
FPC3	9.5	0.32	0.375	9.5
FPC4	9.5	0.34	0.350	8.0
MPC1	12.5	0.28	0.400	12.9
MPC2	12.5	0.30	0.395	12.0
MPC3	12.5	0.32	0.390	11.1
MPC4	12.5	0.34	0.380	9.7
CPC1	19.5	0.28	0.410	15.1
CPC2	19.5	0.30	0.405	14.5
CPC3	19.5	0.32	0.400	14.0
CPC4	19.5	0.34	0.390	12.5

simulated data.

RESULTS AND DISCUSSION

Effect of W/C and aggregate size

Table 4 shows the average measured properties of all PC mixes, including permeability coefficient and porosity. It can be seen from Table 4 that the highest permeability coefficient achieved in this study is 15.1 mm/s for mixture CPC1, which was produced from coarse aggregate. Mixture FPC4 has the lowest permeability coefficient of 8 mm/s, which was produced from fine aggregate.

Results indicated that reduction in permeability coefficient caused by size of aggregate was more than that by W/C. The W/C and its effects on PC mixes were evaluated in lab mixes by W/C of 0.28, 0.3, 0.32 and 0.34. Results show good relationship between permeability coefficient and W/C, supporting the conclusion that greater workability leads to a denser specimen with smaller permeability coefficient. Lab mixes had the highest permeability coefficient, had the lowest W/C.

ANN modeling

In this study 65% of data was used for model training and the remaining 35% are used for testing. Accordingly, the data are normalized according to the following formula and is then used in the neural networks.

$$y_i = \frac{x_i}{x_{max}} \ , \ i = 1,2,\dots,n \qquad (5)$$

Where y_i is the normalized data, x_i is the input data, and x_{max} is the maximum of the input data.

The process of network training is accomplished by a feedback propagation algorithm. This algorithm is based on the error-correction learning rule of Liebenberg-Marquardt. The activation function is hyperbolic tangent sigmoid type. This neural networks model has one input layer, one output layer, and one hidden layer.

Modeling of permeability coefficient by ANN; In order to predict the permeability coefficient values for aggregate size and W/C, the following relation was used;

$$\text{permeability coefficient} = f\left(aggregate\ size, \frac{w}{c}\right) \qquad (6)$$

The Importance factor and goodness-of-fit test results of permeability coefficient modeling using ANN are presented in Tables 5 and 6.

The relationship between the W/C and permeability coefficient was analyzed by performing ANN modeling. The results indicate a satisfactory trend as the W/C increased with decrease in permeability coefficient. In same W/C, Results shows that permeability coefficient of FPC are smaller than permeability coefficient of MPC and CPC. For a fixed W/C, sample making by coarse aggregate lead to an increase of permeability coefficient higher than 40%. This increase has seen in other W/C and has proved the important role of aggregate size.

The experimental and ANN simulated data of permeability coefficient in terms of W/C content for different aggregate size are shown in Figures 4 to 6, respectively. In these figures, ANN simulated data are connected by using polynomial form.

Figure 4 illustrates the effect of W/C on permeability coefficient for FPC. The permeability coefficient of FPC generally decreases when the W/C increases. The highest permeability coefficient of around 11.3 mm/s can be seen when the porosity is higher than 39%. Small changes in W/C content can lead to higher changes in permeability coefficient of samples.

The effect of W/C on permeability coefficient for MPC is shown in Figure 5. The highest permeability coefficient of

Table 5. The importance of each factor for ANN modeling.

Factor	Importance	Normalized importance (%)
Aggregate size	0.599	100
W/C	0.401	67

Table 6. The goodness-of-fit results of modeling based on ANN.

Mode	Data used (%)	Relative error
Training	65	0.024
Testing	35	0.017

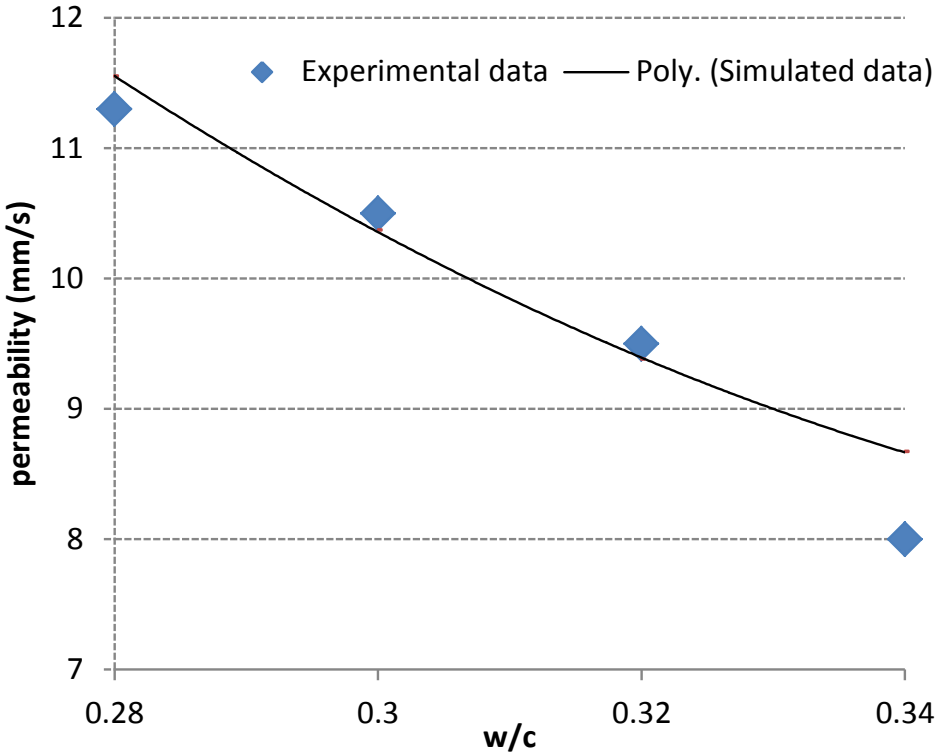

Figure 4. Experimental and simulated values of permeability coefficient with ANN for FPC influence by W/C.

12.9 mm/s can be seen when the porosity is higher than 40% for MPC1. The smallest permeability coefficient of 9.7 mm/s can be seen when the porosity is higher than 38% for MPC4.

The effect of porosity on permeability coefficient for CPC is shown in Figure 6. The highest permeability coefficient of 15.1 mm/s can be seen when the porosity is higher than 41% for CPC1. The smallest permeability coefficient of 12.5 mm/s can be seen when the porosity is higher than 39% for CPC4.

The low workability of PC indicates that the cement paste may have been stiff, and therefore may not have readily coated the pore in the mix. This lower density resulted in a greater amount of pore space available for water to pass through. This would also have contributed to the lower compressive strength. The higher W/C would have contributed to an increased workability as well as made more water available for hydration of the cement paste, resulting in a stronger concrete specimen.

Figure 7 shows experimental value and simulated value for permeability. It can be concluded from Table 6 and Figure 7 that permeability can be efficiently modeled by

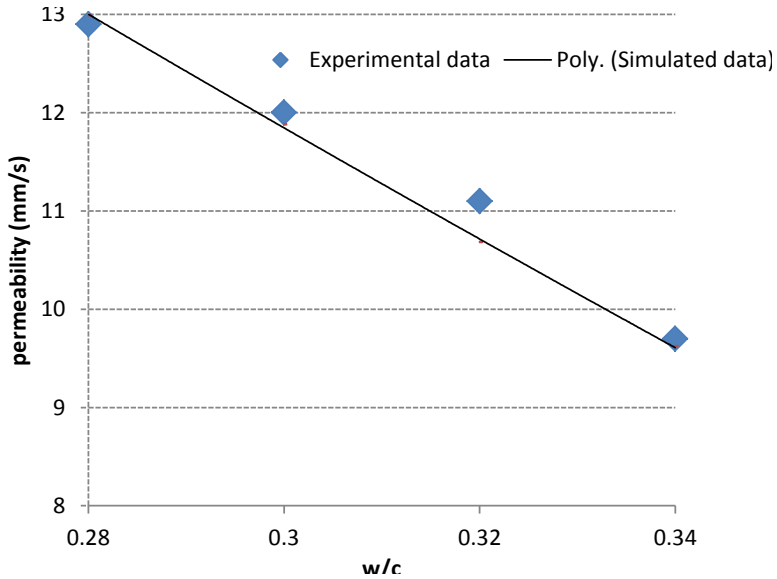

Figure 5. Experimental and simulated values of permeability coefficient ANN for MPC influence by W/C.

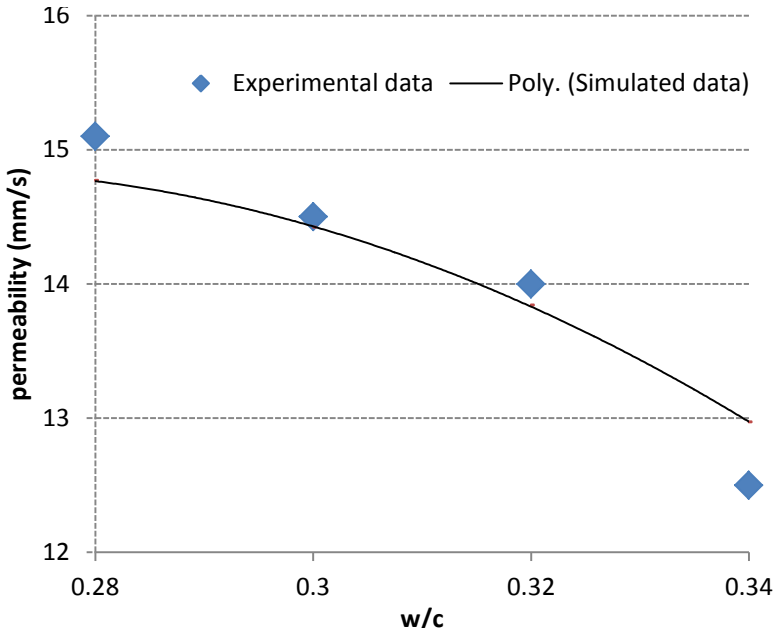

Figure 6. Experimental and simulated values of permeability coefficient with ANN for CPC influence by W/C.

ANN. Furthermore, it was shown that the prediction permeability in fine aggregate was more accurate, it is because of decreasing of porosity.

SUMMARY AND CONCLUSIONS

In this study, the main properties of PC containing three aggregate sizes were investigated. Thirty-six (36) different mixes of PC were tested. The W/C and aggregate size had an effect on the hydrological properties like permeability coefficient and porosity. ANN revealed good relationships between W/C and permeability coefficient for PC. ANN can be used to simulate the influence of aggregate size and W/C on permeability coefficient of PC. The main conclusion

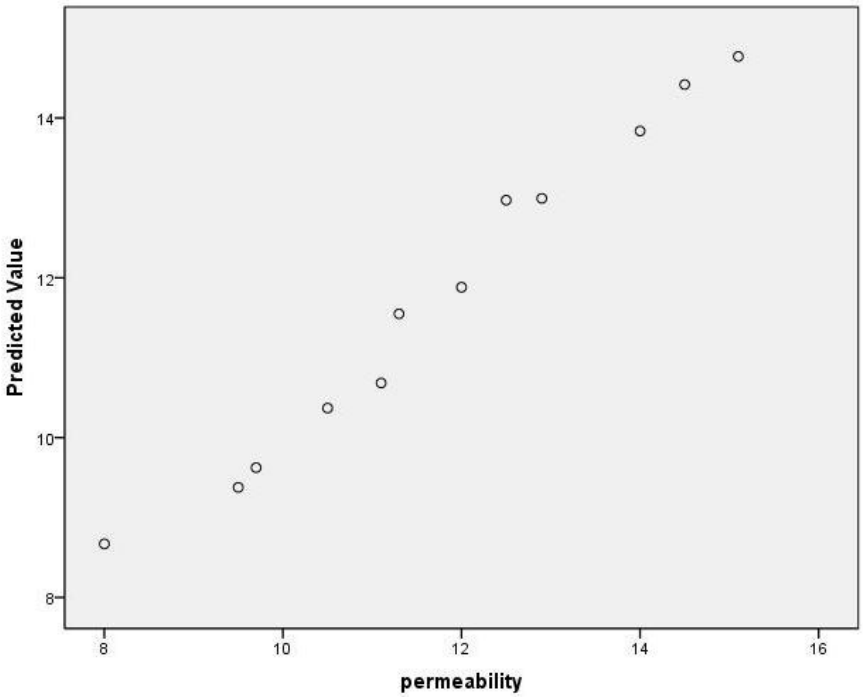

Figure 7. Experimental values versus simulated values of permeability coefficient with ANN.

remarks are summarized as follows:

1. The average water permeability coefficient of PC produced from single size aggregate is approximately 10 mm/s for FPC, 10.5 mm/s for MPC and 13 mm/s for CPC. If the size of aggregates increased then the porosity and permeability coefficient increase too.
2. As expected, if the W/C of PC increased, the porosity and permeability coefficient decrease.
3. ANN indicates that for permeability coefficient of PC samples, the W/C and size of aggregate are significant.
4. The average density of PC was around 1800 kg/m^3 with a porosity of 37%.
5. Since the RMSE of the modeling results is less than 2%, it can be concluded that the ANN can be used as an accurate and fast tool for modeling the permeability coefficient test results.
6. This study also showed that the permeability coefficient can be easily ANN-modeled by using W/C data.

Conflict of interests

Abolfazl Hassani on behalf of other author confirms that there is not any known conflicts of interests associated with this publication and there has been no significant financial support for this work that could have influenced its outcome.

ACKNOWLEDGEMENT

The authors gratefully acknowledge the support given by the laboratory team of the Tarbiat Modares University for their help to complete the laboratory tests and data collection.

REFERENCES

ASTM C 192 (2003). Standard practice for making and curing concrete test specimens. Annual book of ASTM standards 4.02. West Conshohocken, PA: ASTM international.

Boyer M, Haselbach L, Cofer W (2012). Heat transfer finite element modeling in pervious concrete: Impacts of vertical porosity distributions. Transportation Research Board 91th Annual Meeting. January, Washington D.C.

Consolazio GR (2000). Iterative equation solver for bridge analysis using neural networks. Comput.-Aided Civ. Infrastruct. Eng. 15(2):107-119.

Hajela P, Berke L (1991). Neurobiological computational models in structural analysis and design. Comput. Struct. 41(4):657-667.

Hola J, Schabowicz K (2005). Application of artificial neural networks to determine concrete compressive strength based on non-destructive test. J. Civ. Eng. Manag. 11(1):23-32.

Lian C, Zhuge Y (2010). Optimum mix design of enhanced permeable concrete-An experimental investigation. Constr. Build. Mater. 24(1):2664-2671.

Mansour MY, Dicleli M, lee YJ, Zhang J (2004). Predicting the shear strength of reinforced concrete beam using artificial neural networks. Eng. Struct. 26(4):781-799.

Montes F, Valavala S, Haselbach LM (2005). A new test method for porosity measurements of Portland cement pervious concrete. J. ASTM Int. 2(1):1-13.

Montes F, Haselbach L (2006). Measuring hydraulic conductivity in pervious concrete. Environ. Eng. Sci. 23(2):960-9.
Park SB, Tia M (2004). An experimental study on the water-purification properties of porous concrete. Cem. Concr. Res. 34(2):177-184.
Schaefer V, Wang K, Suleiman M, Kevern J (2006). Mix design development for pervious concrete in cold weather climates. Final report, National centre of concrete pavement technology, Iowa state university, Ames, IA.
Shen S, Burton M, Jobson B, Haselbach L (2012). Pervious concrete with titanium dioxide as a photo catalyst compound for a greener urban road environment. Transportation Research Board 91th Annual Meeting. January, Washington D.C.
Shu X, Huang B, Wu H, Dong Q, Burdette EG (2011). Performance comparison of laboratory and field produced pervious concrete mixtures. Constr. Build. Mater. 25(1):3187-3192.
Sumanasooriya MS, Neithalath N (2011). Pore structure features of pervious concrete proportioned for desired porosities and their performance prediction. Cem. Concr. Compos. 33(2):778-787.
Suozzo M, Dewoolkar M (2012). Long-term field monitoring and evaluation of maintenance practice of pervious concrete pavements in Vermont. Transportation Research Board 91th Annual Meeting. January, Washington D.C.
Tho-in T, Sata V, Chindprasirt P, Jaturapitakkul C (2012). Pervious high clacium fly ash geo-polymer concrete. Constr. Build. Mater. 30(2):366-371.
Vancura M, Mc Donald K, Khazanovich L (2011). Microscopic analysis of paste and aggregate distress in pervious concrete in a wet, hard freeze climate. Cem. Concr. Compos. 33(2):1080-1085.
Vassilikou F, Kringos N, Kotsovos Scarpes A (2011). Application of pervious concrete for sustainable pavements: A Micro-Mechanical Investigation. Transportation Research Board 90th Annual Meeting. January, Washington D.C.

academicJournals

Vol. 10(17), pp. 570-578, 15 September, 2015
DOI: 10.5897/SRE2015.6317
Article Number: 412A39E46900
ISSN 1992-2248

http://www.academicjournals.org/SRE

Scientific Research and Essays

Full Length Research Paper

Predicting the permeability of pervious concrete pavement using artificial neural networks modeling

Hassan Tajik Ghashghaei and Abolfazl Hassani*

Department of Civil Engineering and Environment, Tarbiat Modares University, Tehran, Iran.

Received 15 August, 2015; Accepted 2 September, 2015

Pervious concrete (PC) pavement is a sustainable type of concrete pavement that can protect and restore natural ecosystem. The permeability coefficient is the most important characteristic of PC. The purpose of this experimental study was to investigate the effect of mixture design parameters, particularly water-to-cement ratio (W/C) and size of aggregate on the permeability coefficient of PC. The thirty six mixtures were made with W/C in range of 0.28 to 0.34, 350 kg/m^3 cement content and 9.5 to 19.5 mm maximum size of aggregate. In this study the feasibility of using the artificial neural networks (ANN) in predicting the effect of aggregate size and W/C on amount of permeability coefficient of PC was investigated. For modeling, 65% of data was used for model training and remaining 35% was used for model testing. Based on the lowest root mean squared error (RMSE), the best ANN model was chosen. The results showed that the W/C and aggregate size are key parameter, which significantly affect the performance of PC. The ANN modeling was developed in this study can facilitate prediction permeability coefficient of PC. This approach can reduce the number of trial batches for target performance of samples.

Key words: Pervious concrete, artificial neural network, permeability coefficient.

INTRODUCTION

Pervious concrete (PC) is a special type of concrete characterized by an interconnected pore structure and high void content, thus allowing infiltration of water through its structure. While its constituent materials are similar to that of normal concrete, PC contains little or no fine aggregate. It is also known as permeable concrete, porous concrete and no-fine concrete. PC has been used in low-traffic pavements such as parking lots and sidewalks (Schaefer et al., 2006). Permeability coefficient or hydraulic conductivity is the most important performance characteristic of PCs, and with any some material, transportation property are dependent on the pore structure features (Montes and Haselbach, 2006). The PC allows water to pass through its structure due to an increased air voids network. This open structure gives this concrete the added possibility to be applied in pavement engineering as a water drainage layer (Vassilikou et at., 2011). The costs of such asphalt pavements will grow the coming years due to the foreseeable increase in oil prices. PC is therefore a suitable material to be considered for increased usage in the developing sustainable pavement (Lian and Zhuge,

*Corresponding author. E-mail: hassani@modares.ac.ir

Table 1. Engineering properties of aggregates.

Flakiness Index (%) (BS-812)	Water absorption (%) (AASHTO T-85)	Los Angeles abrasion (%) (AASHTO T-96)	Sand equivalent (%) (AASHTO T-176)
10	3	13	70

Table 2. The Chemical properties of cement Type 2, according to ASTM C150 (Tehran Cement Co. Specification).

Constituent compounds	CaO, %	SiO_2, %	Al_2O_3, %	Fe_2O_3, %	MgO, %	SO_3, %	L.O.I, %	I.R, %
Measured value	63.35	21.45	4.61	3.3	2.26	2.05	2.00	0.57

2010; Vancura, 2011; Sumanasooriya and Neithalath, 2011). Natural resources are increasingly consumed due to rapid urbanization and there after human construction activities, so that various strategies are being investigated by engineers to protect and restore natural ecosystems in the world. PC pavement is termed as comprising material that facilitate storm water infiltrate and transfer to the underlying subsoil (Suozzo and Dewoolkar, 2012; Shu et al., 2011).

The porosity is the ratio of the volume of voids to the total volume of the specimen. Some of the voids in PC are not effective in carrying water through the material. The voids, which are frequently called the 'effective voids' are important. Some methods for finding the porosity of PC only calculate the effective voids (Boyer et al., 2012; Shen et al., 2012; Tho-in et al., 2012). Some researchers recommends to finding the total porosity of PC using a water displacement method. The water displacement method is based on Archimedes principle of buoyancy, which states that the buoyancy force is equal to the weight of fluids displaced. In this method, the dry mass, submerged mass and the total volume must be known to calculate the porosity (Montes et al., 2005).

Since the permeability coefficient of PC is the most important characteristic of PC, in this experimental study, the characteristic of PC has been evaluated. It's believed that PC can effectively assist solving drainage problems and reducing the risk of flash flooding, resulting from continuous urban development. The most important mixture design parameters for PC that affect the performance and workability are aggregate size and water-to-cement ratio (W/C). PC made with different W/C has different permeability coefficient. In this study an ANN modeling approach was used to determine the effect of aggregate size and W/C on permeability coefficient of PC.

EXPERIMENTAL PROGRAM

Materials and mixtures

A total of thirty-six PC samples were prepared and tested to determine the porosity content and permeability coefficient. The compositions used to prepare PC samples in this study consisted aggregates, ordinary Portland cement, and water.

All mixtures were designed with single size of crushed silica aggregates. The single size of aggregate defined as the size of sieve on which, 100% of aggregate was passed but all retained the sieve under that. Crushed silica aggregates with a size of 4.75-9.5, 9.5-12.5 and 12.5-19.5 mm were used in this study. Aggregates with a size of 4.75-9.5 mm were named fine and aggregates with a size of 9.5-12.5 mm were named medium and aggregates with a size of 12.5-19.5 mm were named coarse. Using single size aggregates for making samples, leads to gain higher porosity content. However, this approach reduces the workability of samples. The used aggregates were from the eastern area of Tehran. Three groups of samples for this study were developed. The first group was produced with only coarse aggregates with one grading (12.5-19.5 mm). The second group was produced with medium aggregates with one grading (9.5-12.5 mm). The third group was produced with fine aggregates with one grading (4.75-9.5 mm). The engineering properties of used aggregates are shown in Table 1.

For preparing all the PC mixtures, type 2 Portland cement was used. The chemical properties of used cement are shown in Table 2. The physical properties of used cement are shown in Table 3. All mixtures were produced by using single size aggregate and Portland cement with W/C of 0.28, 0.3, 0.32, and 0.34. 1400 kg of aggregates was used for making one cubic meter of PC mixes. The cement content of all the mixtures was around 350 kg/m^3. The W/C was incrementally changed from 0.28 to 0.34. In this way, samples of different porosity were obtained. PC mixes were made from fine aggregates was named Fine PC (FPC), PC mixes were made from medium aggregates was named Medium PC (MPC), and PC mixes were made from coarse aggregates was named Coarse PC (CPC). This division was used to compare the performance of PC mixes made from different aggregates size.

For making samples, materials were mixed in a rotating-drum mixer. For each mixture, triplicates of 100 × 200 mm cylinders were prepared. The fresh concrete was compacted in molds in three layers same to the one described in ASTM C 192; *Practice for making and curing concrete test specimens in the laboratory*. Instead of mechanical vibration because of the risk of blockage of the PC open pore structure, each layer tamped 15 times using a standard compacting bar. Excess concrete above the upper edge of the mold, was removed and a steel trowel was used to press on the surface for levelling. All specimens were de-molded after 24 h and stored in the curing room at 95% relative humidity.

Density test was performed for hardened concrete samples by simple dimensional checks, followed by weighting and calculation. The average density was 1800 kg/m^3 with a porosity of 37%. Picture of sample for permeability coefficient test is shown in Figure 1.

Table 3. The physical properties of cement type 2, according to ASTM C150 (Tehran Cement Co. Specification).

	Chemical properties			Blaine specific surface, cm^2/g	Autoclave expansion, %	Physical properties Setting time		Compressive strength MPa		
	Mg O%	L.O. I%	I.R %			Initial minutes	Final hours	3-day	At least 7 days	At last 28 days
Value	<6	<3	<0.75	>2800	<0.8	>45	<6	>10	>17	>21

Figure 1. PC Sample for permeability coefficient test.

Testing procedure

Permeability test

The permeability coefficient test was measured using the falling head method. Permeability coefficient was calculated using the Darcy's law as gives:

$$k = (A_1 l)/(A_2 t)\log(h_1/h_2) \quad (1)$$

Where A_1 and A_2 are the cross-sectional areas of the sample and the tube respectively, and L is the length of the specimen for typical specimen geometry, h_1 or h_2 are the initial and final heads of water and t is the time between transition water from h_1 to h_2. Picture of permeability coefficient test kit is shown in Figure 2.

The specimens were enclosed in a mold that was lined with a thin rubber sheet, and tightened with house clamps to minimize any flow along the sides of the mold that would affect the measurement of permeability coefficient. The sample was then connected to a vertical PVC pipe on both the upstream and downstream sides.

The apparatus was filled with water from the downstream end, to expel any air voids that may have been present in the PC sample. Once water head reached the top of the specimen, the apparatus was then filled from the upstream side. The system was allowed to reach equilibrium, at which time the water level was recorded, representing the head level on the downstream side. Maintaining the constant downstream head at a higher elevation than top of the PC sample provided full saturation throughout the test. The upstream water level was then increased to a height of 30 cm and the valve closed. The valve was then opened and water allowed to fall to a height of 10 cm, during which the time it look for the water level to fall was recorded. This head difference was expected to maintain laminar flow for the range of anticipated permeability coefficient.

Porosity test

The total porosity was measured by finding the difference of the PC sample cylinder weight submerged in the water and the weight after air drying for 24 h. The difference in the measured weights was then divided by the sample volume (mm^3) as follow (Park and Tia, 2004):

$$p = 1 - (((w_1 - w_2)/\rho_w)/v) * 100 \quad (2)$$

Where p is the total porosity of the PC (%), w_1 is the PC sample weight air-dried for 24 h (kg), w_2 is the PC sample weight submerged under water (kg), v is the PC sample volume (mm^3), and ρ_w is density of water (kg/mm^3).

Artificial neural networks

ANNs are data processing systems consisting of a large number of simple, highly interconnected processing elements (artificial neurons) in an architecture inspired by structure of the central cortex of the brain (Hola and Schabowicz, 2005; Mansour et al., 2004). Much of success of neural network is due to such characteristic as nonlinear processing and parallel processing. Neural networks model techniques have been rapidly applied in engineering, business, psychology, science, and medicine in recent years. In civil engineering the methodology of neural networks has been successfully applied to a number of areas such as structural analysis and design (Hajela and Berke, 1991; Consolazio, 2000).

In this study for ANN modeling, the multilayer perception (MLP) is

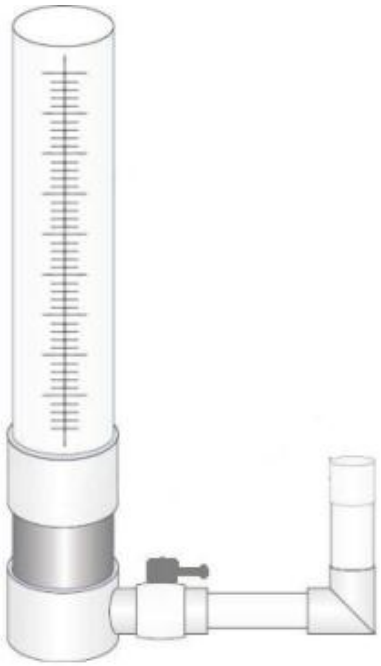

Figure 2. Falling head method kit for permeability coefficient measurement.

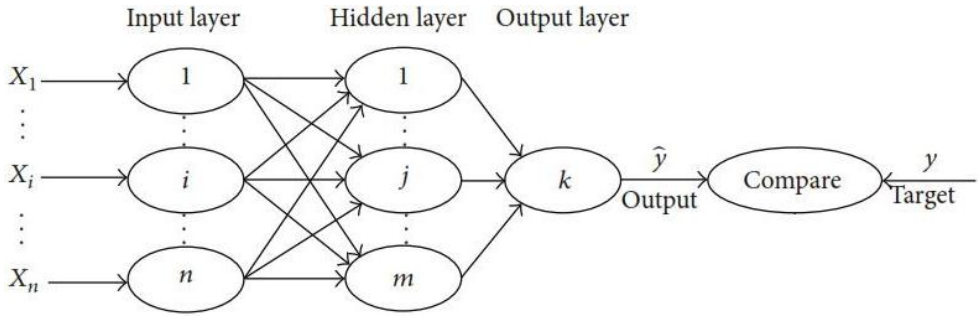

Figure 3. General framework of three-layered neural networks.

used. MLP is a feed forward artificial neural network model. MLP consists of multiple layers of nodes in a directed graph, with each layer fully connected to the next one. Three-layered ANN shown in Figure 3 was used in this study.

Three-layered feed forward neural networks (FFNN) are based on a linear combination of the input variables, which are transformed by a nonlinear activation function. The explicit expression for an output value of ANN is given by following equation:

$$y_k = f_o\left(\sum_{j=1}^{m} w_{kj}.f_h.\left(\sum_{i=1}^{n} w_{ji}.x_i + w_{jo}\right) + w_{ko}\right) \quad (3)$$

Where w_{ji} is the weight in the hidden layer connecting the ith neuron in the input layer and jth neuron in the hidden layer; w_{jo} is the bias for jth hidden neuron; f_h is the activation function of the hidden neuron; w_{kj} is the weight in the output layer connecting the jth neuron in the hidden layer and the kth neuron in the output layer; w_{ko} is the bias for the kth output neuron; f_o is the activation function for the output neuron. The weights are different in the hidden and output layer, and their values can be changed during the process of network.

To examine how close the predicted data to the experimental ones, some different criteria are used. There are two types of graphical and statistical criteria goodness of fit where each has its own unique features, and is used for a specific purpose. Since the graphical method is not accurate and varies depending on opinion of individual person, the statistical criteria were used in this study. Root mean square error (RMSE) is the most widely used statistical criteria. Finally, the best model, based on the lowest root mean square error coefficient, is chosen;

$$\mathrm{RMSE} = \left(\frac{1}{n}\sum_{i=1}^{n} (x_s - x_e)^2\right)^{0.5} \quad (4)$$

Where n is the number of data, x_e is experimental data, and x_s is

Table 4. All PC mixes measured properties.

PC mixtures	Size of aggregates (mm)	W/C	Porosity	Permeability coefficient (mm/s)
FPC1	9.5	0.28	0.390	11.3
FPC2	9.5	0.30	0.386	10.5
FPC3	9.5	0.32	0.375	9.5
FPC4	9.5	0.34	0.350	8.0
MPC1	12.5	0.28	0.400	12.9
MPC2	12.5	0.30	0.395	12.0
MPC3	12.5	0.32	0.390	11.1
MPC4	12.5	0.34	0.380	9.7
CPC1	19.5	0.28	0.410	15.1
CPC2	19.5	0.30	0.405	14.5
CPC3	19.5	0.32	0.400	14.0
CPC4	19.5	0.34	0.390	12.5

simulated data.

RESULTS AND DISCUSSION

Effect of W/C and aggregate size

Table 4 shows the average measured properties of all PC mixes, including permeability coefficient and porosity. It can be seen from Table 4 that the highest permeability coefficient achieved in this study is 15.1 mm/s for mixture CPC1, which was produced from coarse aggregate. Mixture FPC4 has the lowest permeability coefficient of 8 mm/s, which was produced from fine aggregate.

Results indicated that reduction in permeability coefficient caused by size of aggregate was more than that by W/C. The W/C and its effects on PC mixes were evaluated in lab mixes by W/C of 0.28, 0.3, 0.32 and 0.34. Results show good relationship between permeability coefficient and W/C, supporting the conclusion that greater workability leads to a denser specimen with smaller permeability coefficient. Lab mixes had the highest permeability coefficient, had the lowest W/C.

ANN modeling

In this study 65% of data was used for model training and the remaining 35% are used for testing. Accordingly, the data are normalized according to the following formula and is then used in the neural networks.

$$y_i = \frac{x_i}{x_{max}} \quad , \quad i = 1,2,\dots,n \qquad (5)$$

Where y_i is the normalized data, x_i is the input data, and x_{max} is the maximum of the input data.

The process of network training is accomplished by a feedback propagation algorithm. This algorithm is based on the error-correction learning rule of Liebenberg-Marquardt. The activation function is hyperbolic tangent sigmoid type. This neural networks model has one input layer, one output layer, and one hidden layer.

Modeling of permeability coefficient by ANN; In order to predict the permeability coefficient values for aggregate size and W/C, the following relation was used;

$$\text{permeability coefficient} = f\left(aggregate\ size, \frac{w}{c}\right) \qquad (6)$$

The Importance factor and goodness-of-fit test results of permeability coefficient modeling using ANN are presented in Tables 5 and 6.

The relationship between the W/C and permeability coefficient was analyzed by performing ANN modeling. The results indicate a satisfactory trend as the W/C increased with decrease in permeability coefficient. In same W/C, Results shows that permeability coefficient of FPC are smaller than permeability coefficient of MPC and CPC. For a fixed W/C, sample making by coarse aggregate lead to an increase of permeability coefficient higher than 40%. This increase has seen in other W/C and has proved the important role of aggregate size.

The experimental and ANN simulated data of permeability coefficient in terms of W/C content for different aggregate size are shown in Figures 4 to 6, respectively. In these figures, ANN simulated data are connected by using polynomial form.

Figure 4 illustrates the effect of W/C on permeability coefficient for FPC. The permeability coefficient of FPC generally decreases when the W/C increases. The highest permeability coefficient of around 11.3 mm/s can be seen when the porosity is higher than 39%. Small changes in W/C content can lead to higher changes in permeability coefficient of samples.

The effect of W/C on permeability coefficient for MPC is shown in Figure 5. The highest permeability coefficient of

Table 5. The importance of each factor for ANN modeling.

Factor	Importance	Normalized importance (%)
Aggregate size	0.599	100
W/C	0.401	67

Table 6. The goodness-of-fit results of modeling based on ANN.

Mode	Data used (%)	Relative error
Training	65	0.024
Testing	35	0.017

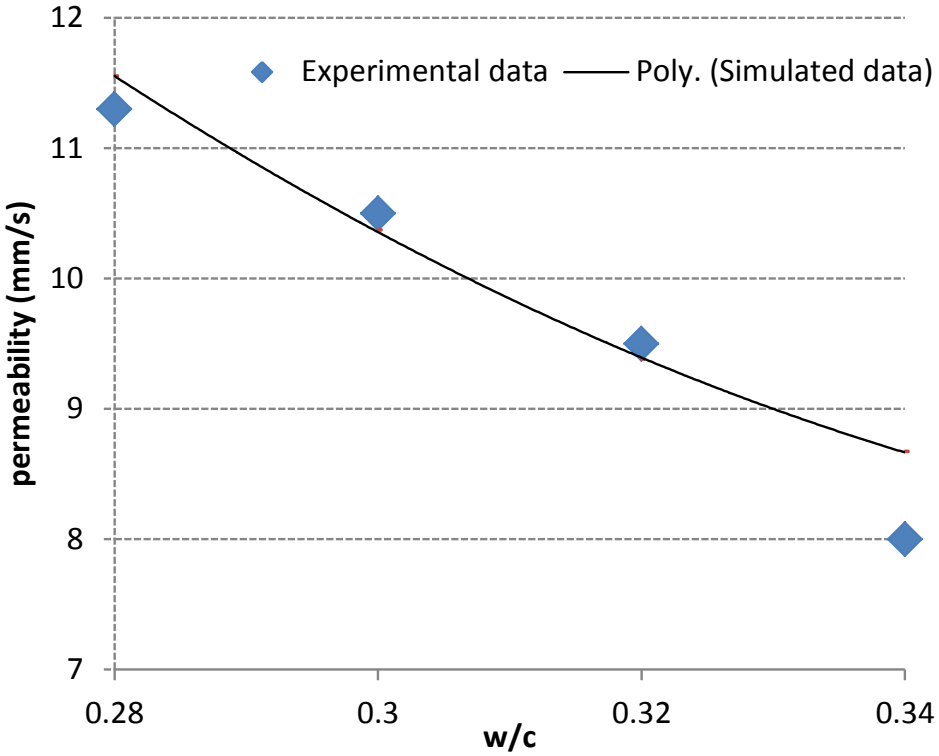

Figure 4. Experimental and simulated values of permeability coefficient with ANN for FPC influence by W/C.

12.9 mm/s can be seen when the porosity is higher than 40% for MPC1. The smallest permeability coefficient of 9.7 mm/s can be seen when the porosity is higher than 38% for MPC4.

The effect of porosity on permeability coefficient for CPC is shown in Figure 6. The highest permeability coefficient of 15.1 mm/s can be seen when the porosity is higher than 41% for CPC1. The smallest permeability coefficient of 12.5 mm/s can be seen when the porosity is higher than 39% for CPC4.

The low workability of PC indicates that the cement paste may have been stiff, and therefore may not have readily coated the pore in the mix. This lower density resulted in a greater amount of pore space available for water to pass through. This would also have contributed to the lower compressive strength. The higher W/C would have contributed to an increased workability as well as made more water available for hydration of the cement paste, resulting in a stronger concrete specimen.

Figure 7 shows experimental value and simulated value for permeability. It can be concluded from Table 6 and Figure 7 that permeability can be efficiently modeled by

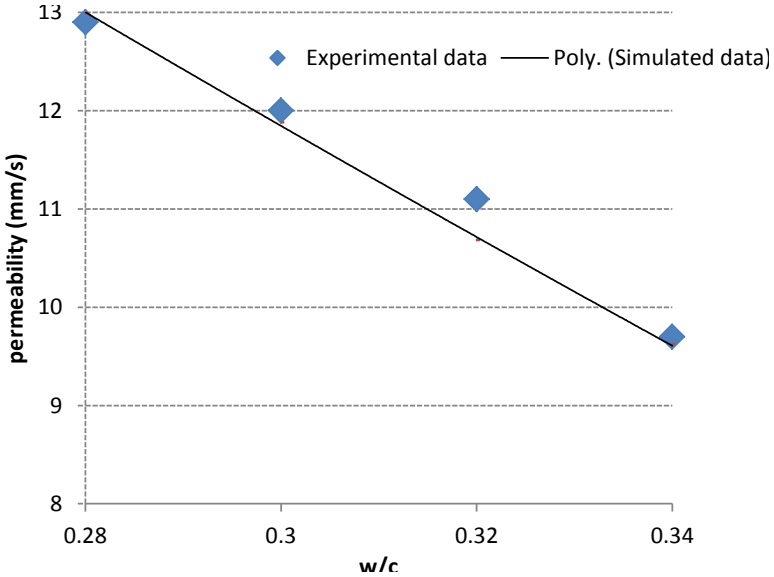

Figure 5. Experimental and simulated values of permeability coefficient ANN for MPC influence by W/C.

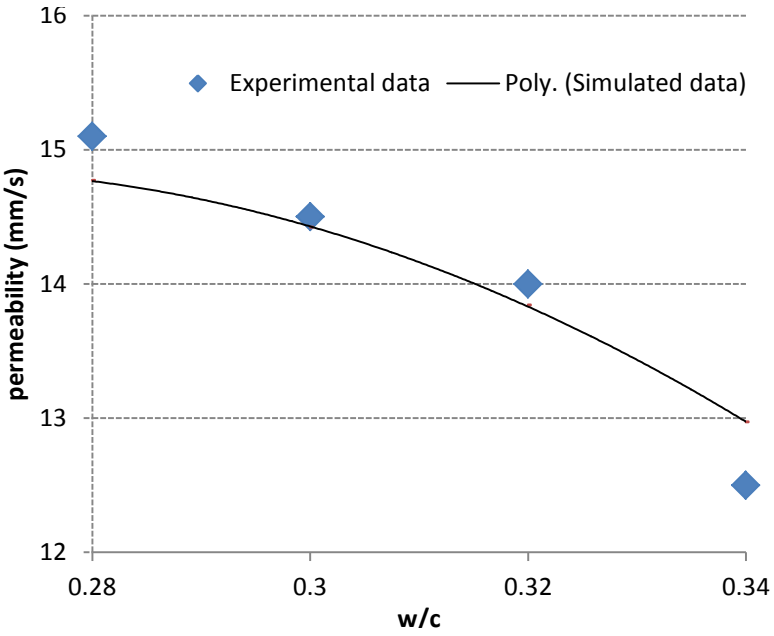

Figure 6. Experimental and simulated values of permeability coefficient with ANN for CPC influence by W/C.

ANN. Furthermore, it was shown that the prediction permeability in fine aggregate was more accurate, it is because of decreasing of porosity.

SUMMARY AND CONCLUSIONS

In this study, the main properties of PC containing three aggregate sizes were investigated. Thirty-six (36) different mixes of PC were tested. The W/C and aggregate size had an effect on the hydrological properties like permeability coefficient and porosity. ANN revealed good relationships between W/C and permeability coefficient for PC. ANN can be used to simulate the influence of aggregate size and W/C on permeability coefficient of PC. The main conclusion

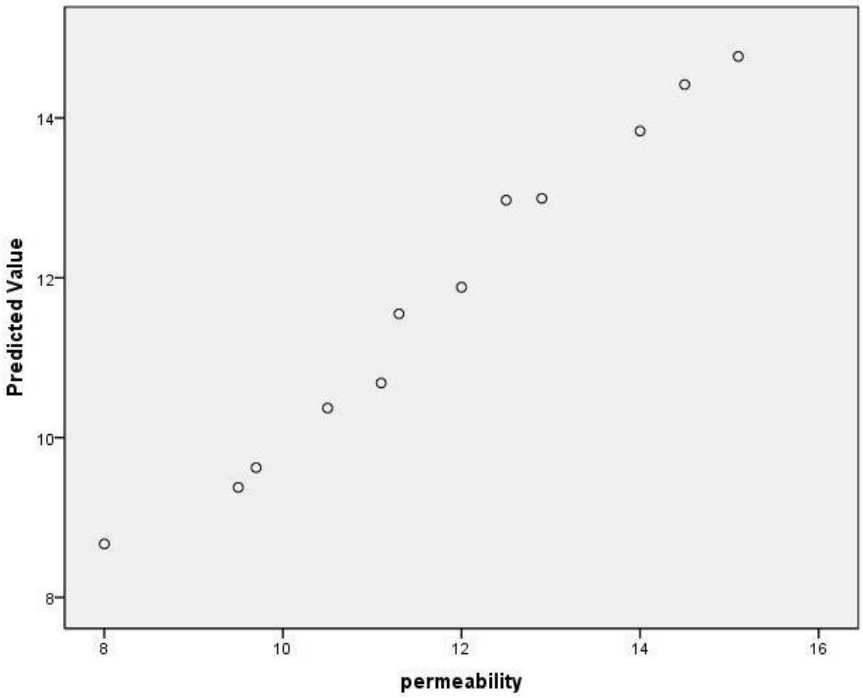

Figure 7. Experimental values versus simulated values of permeability coefficient with ANN.

remarks are summarized as follows:

1. The average water permeability coefficient of PC produced from single size aggregate is approximately 10 mm/s for FPC, 10.5 mm/s for MPC and 13 mm/s for CPC. If the size of aggregates increased then the porosity and permeability coefficient increase too.
2. As expected, if the W/C of PC increased, the porosity and permeability coefficient decrease.
3. ANN indicates that for permeability coefficient of PC samples, the W/C and size of aggregate are significant.
4. The average density of PC was around 1800 kg/m^3 with a porosity of 37%.
5. Since the RMSE of the modeling results is less than 2%, it can be concluded that the ANN can be used as an accurate and fast tool for modeling the permeability coefficient test results.
6. This study also showed that the permeability coefficient can be easily ANN-modeled by using W/C data.

Conflict of interests

Abolfazl Hassani on behalf of other author confirms that there is not any known conflicts of interests associated with this publication and there has been no significant financial support for this work that could have influenced its outcome.

ACKNOWLEDGEMENT

The authors gratefully acknowledge the support given by the laboratory team of the Tarbiat Modares University for their help to complete the laboratory tests and data collection.

REFERENCES

ASTM C 192 (2003). Standard practice for making and curing concrete test specimens. Annual book of ASTM standards 4.02. West Conshohocken, PA: ASTM international.

Boyer M, Haselbach L, Cofer W (2012). Heat transfer finite element modeling in pervious concrete: Impacts of vertical porosity distributions. Transportation Research Board 91th Annual Meeting. January, Washington D.C.

Consolazio GR (2000). Iterative equation solver for bridge analysis using neural networks. Comput.-Aided Civ. Infrastruct. Eng. 15(2):107-119.

Hajela P, Berke L (1991). Neurobiological computational models in structural analysis and design. Comput. Struct. 41(4):657-667.

Hola J, Schabowicz K (2005). Application of artificial neural networks to determine concrete compressive strength based on non-destructive test. J. Civ. Eng. Manage. 11(1):23-32.

Lian C, Zhuge Y (2010). Optimum mix design of enhanced permeable concrete-An experimental investigation. Constr. Build. Mater. 24(1):2664-2671.

Mansour MY, Dicleli M, lee YJ, Zhang J (2004). Predicting the shear strength of reinforced concrete beam using artificial neural networks. Eng. Struct. 26(4):781-799.

Montes F, Valavala S, Haselbach LM (2005). A new test method for porosity measurements of Portland cement pervious concrete. J. ASTM Int. 2(1):1-13.

Montes F, Haselbach L (2006). Measuring hydraulic conductivity in pervious concrete. Environ. Eng. Sci. 23(2):960-9.
Park SB, Tia M (2004). An experimental study on the water-purification properties of porous concrete. Cem. Concr. Res. 34(2):177-184.
Schaefer V, Wang K, Suleiman M, Kevern J (2006). Mix design development for pervious concrete in cold weather climates. Final report, National centre of concrete pavement technology, Iowa state university, Ames, IA.
Shen S, Burton M, Jobson B, Haselbach L (2012). Pervious concrete with titanium dioxide as a photo catalyst compound for a greener urban road environment. Transportation Research Board 91th Annual Meeting. January, Washington D.C.
Shu X, Huang B, Wu H, Dong Q, Burdette EG (2011). Performance comparison of laboratory and field produced pervious concrete mixtures. Constr. Build. Mater. 25(1):3187-3192.
Sumanasooriya MS, Neithalath N (2011). Pore structure features of pervious concrete proportioned for desired porosities and their performance prediction. Cem. Concr. Compos. 33(2):778-787.
Suozzo M, Dewoolkar M (2012). Long-term field monitoring and evaluation of maintenance practice of pervious concrete pavements in Vermont. Transportation Research Board 91th Annual Meeting. January, Washington D.C.
Tho-in T, Sata V, Chindprasirt P, Jaturapitakkul C (2012). Pervious high clacium fly ash geo-polymer concrete. Constr. Build. Mater. 30(2):366-371.
Vancura M, Mc Donald K, Khazanovich L (2011). Microscopic analysis of paste and aggregate distress in pervious concrete in a wet, hard freeze climate. Cem. Concr. Compos. 33(2):1080-1085.
Vassilikou F, Kringos N, Kotsovos Scarpes A (2011). Application of pervious concrete for sustainable pavements: A Micro-Mechanical Investigation. Transportation Research Board 90th Annual Meeting. January, Washington D.C.

academicJournals

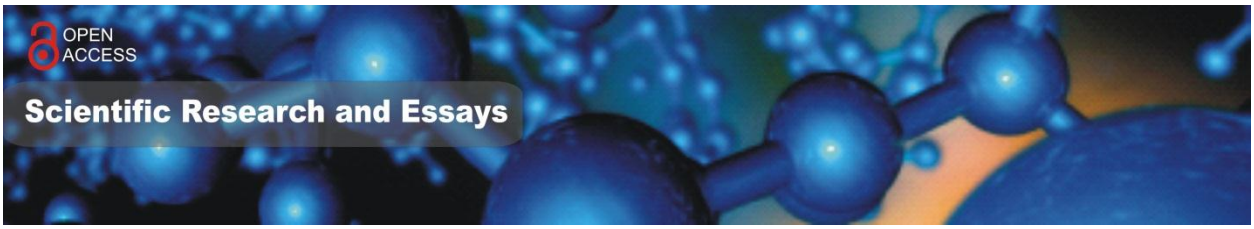

Related Journals Published by Academic Journals

- International NGO Journal
- International Journal of Peace and Development Studies